Mitochondria-Selective Dicationic Small Molecule Ligand Targeting G-Quadruplex Structures for Human Colorectal Cancer Therapy

Bo-Xin Zheng[1], Wei Long[1], Wende Zheng[2], Yaoxun Zeng[2], Xiao-Chun Guo[3], Ka-Hin Chan[1], Meng-Ting She[2], Alan Siu-Lun Leung[1], Yu-Jing Lu[3] and Wing-Leung Wong*[,1,2]

[1] State Key Laboratory of Chemical Biology and Drug Discovery, Department of Applied Biology and Chemical Technology, The Hong Kong Polytechnic University, Hung Hom, Kowloon, Hong Kong SAR 999077, China.

[2] The Hong Kong Polytechnic University Shenzhen Research Institute, Shenzhen 518057, P. R. China.

[3] School of Biomedical and Pharmaceutical Sciences, Guangdong University of Technology, Guangzhou 510006, P. R. China.

* Corresponding author

E-mail: wing.leung.wong@polyu.edu.hk

ABSTRACT

Mitochondria are important drug targets for anticancer and other disease therapy. Certain human mitochondrial DNA sequences capable of forming G-quadruplex structures (G4s) are emerging drug targets of small-molecules. Despite some mitochondria-selective ligands have been reported for drug delivery against cancers, the ligand design is mostly limited to triphenylphosphonium scaffold. The novel ligand designed with lipophilic small-sized scaffolds bearing multi-positive charges targeting the unique feature of high mitochondrial membrane potential (MMP) is lacking and most mitochondria-selective ligands are not G4-targeting. Herein, we reported a new small-sized di-cationic lipophilic ligand to target MMP and mitochondrial DNA G4s to enhance drug delivery for anticancer. The ligand showed markedly alteration of mitochondrial gene expression and substantial induction of ROS production, mitochondrial dysfunction, DNA damage, cellular senescence, and apoptosis. The ligand also exhibited high anticancer activity against HCT116 cancer cells

(IC_{50}, 3.4 μM) and high antitumor efficacy in HCT116 tumor xenograft mouse model (~70% tumor weight reduction).

KEYWORDS

Mitochondrial G-quadruplex DNA; Mitochondria-selective ligand; Human colorectal cancer therapy; Di-cationic ligand; DNA G-quadruplex-targeting ligand

1. INTRODUCTION

The thermodynamically stable G-quadruplex structure (G4) formed *in vitro* from the nucleic acid sequences rich in guanine (G) nucleotides has been proved with *X*-ray crystal structures and well-documented over the past decades;[1-3] however, the *in vivo* existing of G4s and their associated biofunctions in cells are still unclear.[4] Currently, increasing evidence suggest that G4s may play critical roles in genome functions such as replication, transcription, genome stability and epigenetic regulation.[5] The dysregulation of G4-formation in human cells is also found associated with genetic diseases including neurological diseases and cancer.[6-8] Despite the mechanism of G4s causing human diseases is still not clear, G4-selective small molecule ligands capable of stabilizing G4s are recognized as the potential drug candidate for human cancer treatment.[9-12]

Recent studies show that mitochondria are the promising drug target for cancer therapy because mitochondrial metabolism plays critical roles in cancer development and progression[13-15] and in other diseases.[16] DNA G4s are also found in the human mitochondrial genome (mtDNA) and around 170 putative G4-forming mtDNA sequences have been identified.[17-19] Some recent evidence support that these G4-forming sequences may be associated with the origin of mtDNA deletions that may cause diseases in human.[20-22] Moreover, the mtDNA G4-structure (G4-mtDNA) is reported to show close relationship with glycolysis,[23] but how G4-mtDNA regulates the biological process is still unclear. To understand more about the biofunction and regulatory roles of the G4-mtDNA that causes diseases, we need to develop cell-permeable and target-specific fluorescent ligands to visualize the intracellular

G4-mtDNA for chemical biology study[24] and to interrupt the abnormal cellular function of G4s to achieve therapeutic aims such as anticancer.

Mitochondria are essential organelles of living cells to produce energy and they also maintain the cellular homeostasis and regulate cell death pathways.[25-27] Mitochondrial dysfunction is also known to activate several mitochondrial retrograde signaling and mitochondrial stress response pathways, which promote cancer progression to malignancy.[28-30] Therefore, targeting mitochondrial function has emerged as a potential therapeutic strategy against cancer. Currently, several drugs that target mitochondrial metabolism and/or induce mitochondrial apoptosis have been investigated.[31-35] Nevertheless, small molecule ligands specifically targeting G4-mtDNA and capable of regulating mitochondrial metabolism and apoptosis are rarely found. BMVC-12-P,[36] $TMPyP_4$[37] and DODC[37] are the only known example binding to G4-mtDNAs and showing anticancer activity, but their target specificity in living cells has not been investigated. In addition, the molecular scaffold for designing G4-mtDNA-targeting ligands is scarce.[38, 39] Therefore, the development of small molecule ligands with a new molecular design to enhance the cellular delivery and the selectivity targeting mitochondria and G4-mtDNA in living cancer cells are very important.

The triphenylphosphonium (TPP^+) is the most widely used moiety in designing mitochondria-selective ligands for drug delivery in cancer treatment.[34, 40] TPP^+-based agents are mitochondrial membrane targeting; however, the design of ligands based on a lipophilic small-sized molecular scaffold bearing multi-positive charges to target mitochondria that are featured with high mitochondrial membrane potential (MMP, $\Delta\Psi_{mito}$, -150 ~ -180 mV) is currently lacking.[41, 42] In the present study, we designed a new series of di-cationic and lipophilic ligands targeting MMP. The ligand was demonstrated to be mitochondria-selective and G4-mtDNA-targeting with high anticancer potency against human colorectal cancer (CRC). CRC is the third most commonly diagnosed cancer and is the second most deadly cancer at present. It is also one of the tumor types showing less therapeutic effectiveness with immunotherapy.[43] From the cellular results obtained with the ligands, compound **9**, showing excellent selectivity targeting mitochondria and G4-mtDNAs, exhibits high

potency in inhibiting mitochondrial gene expression, downregulating the expression of proteins of respiratory chain complexes I, II, III and IV, dysregulating oxidative phosphorylation and glycolysis, increasing mitochondrial reactive oxygen species (mtROS) level, inducing DNA damage, and causing severe senescence and cell death in human colorectal cancer cells (HCT116). In addition, the high *in vivo* antitumor efficacy and low cytotoxicity of **9** were validated in a HCT116 tumor xenograft mouse model.

2. RESULTS AND DISCUSSION

2.1 The Design of Di-cationic Small-sized Lipophilic Ligands Targeting Mitochondria and G4-mtDNA.

Mitochondria are special organelles, in which the transfer of protons from mitochondrial matrix to mitochondrial intermembrane space by proton pumps creates a highly negative MMP in mitochondrial matrix.[44] For this reason, most mitochondria-targeting ligands are lipophilic and cationic such as TPP^+. Currently, most G4-ligands reported are mono-cationic and nonspecific to mitochondria. Thus, the ligand also enters nucleus and/or other organelles in living cells. Considering the unique feature of high MMP of mitochondria, we rationally designed a series of lipophilic ligands bearing two cationic quinolinium scaffolds that was bridged with a flexible alkyl chain, as shown in Scheme 1, to enhance the cellular selectivity targeting mitochondria. In addition, the quinolinium scaffold was further integrated with a styryl moiety (**1**–**10**) to optimize the G4-selectivity of the ligand. The integration of molecular scaffolds was achieved via a rigid but rotatable ethylene bridge. The two π-conjugated scaffolds may form a co-planar structure upon interacted with targeted G4s and then the adduct can generate intensive fluorescence for real-time imaging and monitoring G4s in living cells.[45] To the best of our knowledge, there is no such small-sized, di-cationic, mitochondria-selective and G4-targeting ligands reported. Furthermore, the di-cationic feature of these ligands may discriminate well the human tumor cells and healthy cells because tumor cells usually

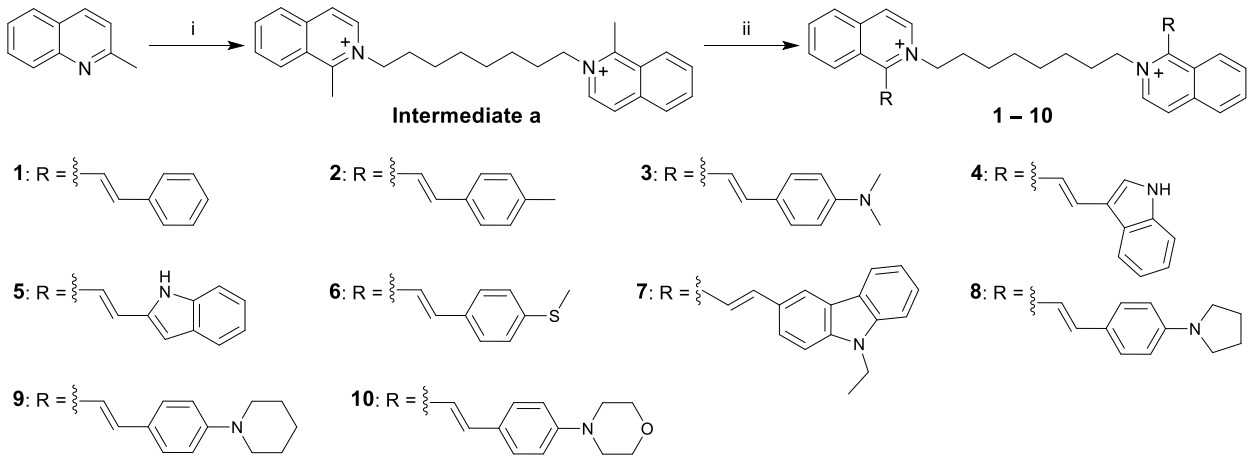

Scheme 1. Synthetic routes to new di-cationic compounds **1–10**. Reaction conditions: (i) 1,8-diiodooctane, ethanol, 100 °C, 24 h; (ii) Selected aldehyde, ethanol, 4-methylpiperidine, 100 °C, overnight.

have a markedly higher MMP. Compared to normal cells, a difference about 60 mV of $\Delta\Psi_{mito}$ was reported in tumor cells,[34, 41, 42] meaning that the more negative MMP of tumor cells could presumably have higher competence to drive more di-cationic small-sized ligands into mitochondria.[46] For proof of concept, two monomeric derivatives, **11** and **12**, shown in Scheme S1, were also synthesized for comparison. The absorption spectra of all ligands synthesized in this study were given in Figure S1.

To search for potent ligands selectively targeting mitochondria and G4-mtDNA for anticancer study, the ligands obtained with high purity (≥ 95%) were investigated comprehensively by determining their sensitivity, selectivity and binding affinity targeting different G4-mtDNA substrates against other nucleic acid structures. In addition, the live-cell imaging and cytotoxicity of ligands against a panel of human cancer cells and noncancerous cells were studied. Firstly, to understand the interaction between these ligands and different nucleic acid substrates, including G4-mtDNAs and non-G4-DNAs, fluorescence titrations were performed to study the sensitivity and selectivity of the ligand towards these substrates in buffer. The results were summarized in Figure S2. It was found that all ligands showed only weak background fluorescence. Upon the ligand interacting with G4-mtDNAs, **3**, **4**, **7**, **8**, **9** and **10** were found able to generate markedly enhanced fluorescence (in most cases, F/F_0 = 10-40 folds). In general, the ligand induce much higher interaction signal for G4-mtDNAs than other nucleic acid substrates, indicating that the ligand is more sensitive towards

G4-mtDNAs. Nonetheless, **3**, **4**, **7** and **8** show relatively low selectivity towards G4-mtDNAs because the intensive fluorescent signals that indicate the ligand interacting with non-G4-DNA substrates are also observed under the same titration conditions (F/F_0 = 2-15 folds generally). We identified that **9** exhibited the best selectivity towards G4-mtDNA substrates (F/F_0 = 12-40 folds; other non-G4-DNAs F/F_0 < 4 folds). These results demonstrate that the integrated styryl moiety (R group) determine the selectivity of the ligand.

Table 1. The affinity (K_D, μM) of ligands binding to G4-mtDNA and non-G4-DNA substrates determined with surface plasmon resonance at 25 °C.

	1	**2**	**3**	**4**	**5**	**6**	**7**	**8**	**9**	**10**
Mito 78	0.29	0.07	0.03	0.08	1.84	0.05	0.02	0.13	0.04	0.12
Mito 55	0.58	0.91	0.13	0.61	0.22	0.46	0.52	0.17	0.17	0.47
Mito 29	0.50	0.72	0.14	0.23	0.14	0.34	0.21	0.15	0.11	0.24
Mito 0.5-16	1.02	1.17	0.11	0.25	> 2	0.15	0.96	0.41	0.29	0.28
HP19	> 2	> 2	> 2	> 2	> 2	> 2	> 2	> 2	> 2	1.86

Table 2. Half-maximal inhibitory concentration (IC_{50}, μM) of ligands against human cancer cell lines (HCT116, LoVo, HeLa, HepG2, MDA-MB-231 and PANC-1) and noncancerous cell lines (HFF1 and BJ) with incubation for 48 h.

	Cancer cells						Noncancerous cells	
	HCT116	LoVo	HeLa	HepG2	PANC-1	MDA-MB-231	HFF1	BJ
1	> 40	> 40	> 40	> 40	> 40	> 40	28.3	> 40
2	27.4	> 40	> 40	> 40	> 40	> 40	> 40	> 40
3	17.2	15.4	29.5	> 40	> 40	> 40	22.7	> 40
4	19.8	> 40	23.3	> 40	> 40	> 40	> 40	> 40
5	8.0	> 40	34.6	37.3	> 40	> 40	> 40	> 40
6	24.7	> 40	> 40	> 40	> 40	> 40	34.8	> 40
7	8.5	> 40	32.1	25.3	> 40	> 40	> 40	> 40
8	5.4	15.0	22.1	> 40	20.5	> 40	31.1	31.4
9	3.4	13.4	23.5	> 40	24.8	34.6	32.7	> 40
10	29.2	35.4	>40	> 40	> 40	> 40	> 40	> 40

Next, we measured the affinity of the ligand binding to G4-mtDNAs in buffer with surface plasmon resonance (SPR). In the assays, four G4-mtDNAs (*Mito 78*, *Mito 55*, *Mito 29* and *Mito 0.5-16*) and a non-G4-DNA (*HP19*) were selected as the model substrates. The affinity obtained was summarized in Table 1. The SPR sensorgrams were given in Figure S3. Most ligands exhibited much stronger affinity towards G4-mtDNAs than non-G4-DNAs. For G4-mtDNA *Mito 78*, the K_D values obtained with most ligands are at nanomolar level (0.02-0.29 μM), while the K_D values for *HP19* are higher than 2 μM, which is at least 6-fold higher than that of G4-mtDNA *Mito 78*. These binding results clearly support that these ligands show stronger affinity with G4-mtDNA substrates. It is noteworthy that the interaction of **9** with the selected G4-mtDNA substrates (*Mito 0.5-16*, K_D = 290 nM; *Mito 29*, K_D = 110 nM; *Mito 55*, K_D = 170 nM; *Mito 78*, K_D = 40 nM) is at least 6-fold stronger than that of the non-G4-DNA (*HP19*, K_D > 2 μM), indicating that **9** is generally selective towards G4-mtDNAs. Moreover, G4-mtDNA substrates including *Mito 29*, *Mito 55*, *Mito 0.5-15*, *Mito 0.5-16*, *Mito 78*, and *Mito 81* (Table S6) were studied with **9** for interactions in solution using isothermal titration calorimetry (ITC) (Figure S4). We found that most K_D values of G4-mtDNA substrates determined were in nanomolar to submicromolar range (0.06-0.27 μM), which was markedly stronger than that of non-G4-DNAs (> 4.7 μM). The results support that **9** may interact with different G4-mtDNA structures with strong affinity.

Cell-based MTT assays were then performed to examine the cytotoxicity of the ligands against a panel of cancer cells and noncancerous cells. The results were summarized in Table 2. The ligands generally show mild toxicity against both human cancer cell lines (HCT116, HeLa, HepG2, MDA-MB-231, PANC-1 and LoVo) and noncancerous cell lines (HFF1 and BJ) and, in most cases, the IC_{50} values obtained are greater than 20 μM; and some are even greater than 40 μM. Notably, **9** shows the highest cytotoxicity against two colorectal cancer cell lines (HCT116, IC_{50} = 3.4 μM; LoVo, IC_{50} = 13.4 μM). On the contrary, **9** exhibits a comparatively mild cytotoxicity against both HFF1 and BJ cells (IC_{50} > 32 μM). The colorectal cancer cells are markedly more susceptible to **9**. Thus, the ligand

could be a potential anticancer agent for treating human colorectal cancer (CRC), which is currently a global challenge in clinical cancer therapy.

To verify the subcellular location of **9** after internalization in living CRC cells (HCT116), we performed live-cell imaging to colocalize the ligand with organelle-specific dyes including Hoechst33342 (nucleus), Lyso-Tracker Blue (lysosome), ER-Tracker Blue (endoplasmic reticulum) and Mito-Tracker Deep Red (mitochondria). The confocal images (Figure S5) reveal that **9** is primarily localized in mitochondria, as indicated by a good colocalization with Mito-Tracker (Pearson's correlation: r = 0.59). Notably, the ligand shows no observable co-localization signal in both nucleus and lysosome, while a weak co-localization signal is found in the endoplasmic reticulum (Pearson's correlation: r = 0.30). The results may support that **9** is mitochondria-selective. The selectivity is most likely due to tailored structural features (di-cationic and small sized) of the ligand that could be more favorable to deliver into mitochondria of cancer cells where have high MMP.[31-35]

As aforementioned, two monomeric analogues, **11** and **12** (Scheme S1), were also synthesized to demonstrate the importance of the di-cationic scaffold design to achieve high intracellular selectivity targeting mitochondria. As shown in Figure S6A, **11** and **12** were also found exhibiting very good selectivity towards G4-mtDNAs over other nucleic acid structures. However, live-cell imaging results reveal that both **11** and **12** are not mitochondria-selective, as indicated clearly by the intensive fluorescent signal observed in the subnuclear region of the cells (Figure S6B). Therefore, these results indicate that the molecular charge may be a critical factor that determines the ability of the ligand to target mitochondria selectively in living cells. In addition, probably due to the monomeric ligands entering nucleus, **11** and **12** may interact with nuclear DNAs and thus they generally exhibit high cytotoxicity against both cancer and noncancerous human cells examined (Table S7).

2.2 The Study of Ligand 9 Interacting with G4-mtDNA Sequences of Mitochondrial Genes Encoding Essential Proteins.

From the above preliminary screening experiments, the best ligand, **9**, was identified to be mitochondria-selective and capable of interacting with different G4-mtDNA structures *in vitro* with

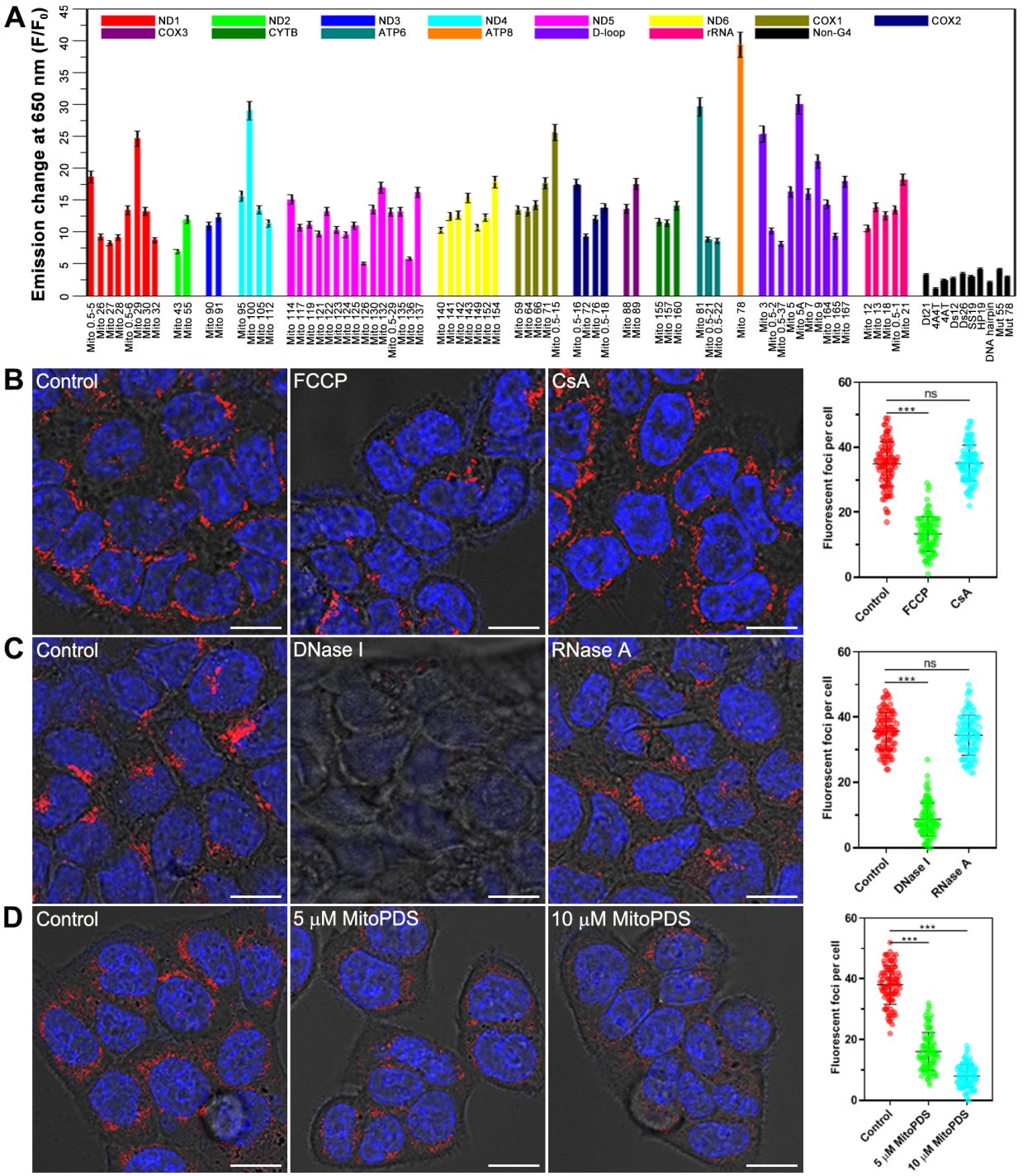

Figure 1. (A) Fluorescence titration experiments. The enhanced fluorescence intensity monitored at 650 nm for the interaction of 5 μM ligand **9** with 20 μM different G4-mtDNA and non-G4-DNA. (B) Single confocal plane images: Living HCT116 cells incubated with 4 μM ligand **9** (λ_{ex}=488 nm) for 1 h and 1 μM Hoechst33342 (λ_{ex}=405 nm) for 30 min after treatment with 1 μM FCCP for 20 min or 1 μM CsA for 24 h. The scale bar is 10 μm. The image magnification is 400x. (C) Single confocal plane images: Living HCT116 cells incubated with 4 μM ligand **9** (λ_{ex}=488 nm) for 1 h and 1 μM Hoechst33342 (λ_{ex}=405 nm) for 30 min, then the cells were fixed and incubated with 200 units RNase A for 3 h or incubated with 200 units DNase I for 3 h. The scale bar is 10 μm. The image magnification is 400x. (D) Single confocal plane images: Living HCT116 cells incubated with 4 μM ligand **9** (λ_{ex}=488 nm) for 1 h and 1 μM Hoechst33342 (λ_{ex}=405 nm) for 30 min, then the cells were treated with MitoPDS at different concentrations for 3 h. The scale bar is 10 μm. The image magnification is 400x. The data are presented as mean ± SEM, and statistical significance is determined by the t test as (ns) not significant, (*) $p < 0.05$, (**) $p < 0.01$, and (***) $p < 0.001$. 100 cells were measured.

strong affinity in nanomolar to submicromolar level. We then investigated its interaction with 71 G4-mtDNA sequences (Table S1) selected from 12 mitochondrial genes encoding essential proteins that were associated with the mitochondrial respiratory chain, mitochondrial D-loop structure, and mitochondrial rRNA. It is because G4-structures formed from these mitochondrial genes are the potential cellular targets of **9**. The stabilization of these G4-structures with **9** may cause mitochondrial dysfunction.

We found that when **9** interacted with various G4-mtDNAs of these mitochondrial genes (Figure 1A), the fluorescent signal was markedly enhanced with respect to the concentration of G4-mtDNA used (Figure S7). In contrast, the fluorescence changes observed for non-G4-DNAs and mutant G4-DNAs (*Mut 55* and *Mut 78*) were much less obvious. UV-Vis titration spectra also show clearly a red-shift peak, indicating that **9** interacts with these G4-mtDNAs to form adducts *in situ* (Figure S8). The non-G4-DNA substrates do not show such obvious red-shift signal in the spectra under the same conditions. We then performed circular dichroism (CD) measurements to study the interaction of **9** and different G4-mtDNAs. The results reveal that the *in vitro* interaction induce signal changes in CD spectra. The CD signal of *Mito 0.5-16* and *Mito 78* at 290 nm is increased evidently. Also, the CD signal of *Mito 81* at 265 nm is increased (Figure S9). These results suggested that **9** may induce G4-formation and stabilize the adduct formed in solution.[47] However, when using non-G4-DNAs (*HP19* and *SS19*), almost no CD signal change was observed.

To further validate the formation of G4-structures for *Mito 78* and *Mito 29* in solution, we performed ^{1}H NMR study. As shown in Figure S10, the characteristic signals of imino protons of *Mito 78* and *Mito 29* G4-structures were found in the region of 10.5-12 ppm in the presence of KCl, while such signals were not observed under the conditions without KCl. The results suggest that both *Mito 78* and *Mito 29* may form G4-structures. Moreover, the interaction between **9** and the G4-structure of *Mito 78* or *Mito 29* was studied preliminary with ^{1}H NMR titrations. With 0.5 and 1 equivalent of **9** added to the solution of *Mito 78* or *Mito 29*, observable proton signal changes were

found. The results indicate that the molecular interaction between **9** and the G4-structure of *Mito 78* or *Mito 29* may be occurred.

To further understand the stability of **9**-G4-mtDNA complex formed *in vitro*, thermal melt CD assays were conducted. As shown in Figure S11, the markedly increased melting points (ΔT_m) in the range of 3.6-16.5 °C were observed; however, the ΔT_m for non-G4-DNAs was only 0.5-2.3 °C. For **9**-G4-mtDNA complexes, such as **9**-*Mito 78* complex (ΔT_m = 11.3 °C) and **9**-*Mito 0.5-16* complex (ΔT_m = 16.5 °C), the ΔT_m values were found much higher. The results support that **9** may interact with G4-mtDNAs and stabilize the complex formed *in vitro*.

Based on the biophysical studies conducted with fluorescence and ^{1}H NMR titrations, CD measurements, thermal melt CD assays, and SPR and ITC binding assays, we have demonstrated that **9** could possibly interact with a number of G4-mtDNA targets including the potential targets formed from 71 DNA sequences selected from 12 important mitochondrial genes as most of them show strong affinity (K_D in submicromolar to nanomolar level) and form stable complexes (ΔT_m, 3.6-16.5 °C) *in vitro*; however, the fact is that it is difficult to confirm which G4-targets of mitochondrial genes actually interacting with the ligand in living cells and *in vivo*. It is because the intracellular folding of G4s is a transient process,[48] and currently, it has not been clear yet. Nonetheless, the biological influence and anticancer mechanism of **9** targeting mitochondria in HCT116 cells were comprehensively investigated in this study.

2.3 Investigation of the Potential Binding Target of Ligand 9 in Living HCT116 Cells.

The *in vitro* results support that **9** is highly selective binding to G4-mtDNAs. We have also verified that **9** is primarily located in mitochondria but not nucleus in HCT116 cells with confocal live-cell imaging assays (Figure S5). Moreover, to increase the concentration of **9** in live-cell imaging assays, it did not change the cellular location of **9** (Figure S12A). Also, increasing the incubation time from 1 to 12 h in living cells, it showed no observable red fluorescence in nucleus (Figure S12B), indicating that **9** is highly mitochondria-selective.

We then studied how ligand **9** was delivered into mitochondria. We previously proposed that the high negative MMP of cancer cells could be a favorable factor to drive the ligand into mitochondria. To verify that MMP is the main driving force for the delivery, a potent uncoupler of mitochondrial oxidative phosphorylation carbonyl cyanide 4-(trifluoromethoxy)phenylhydrazone (FCCP) is utilized to depolarize the MMP of HCT116 cells.[49] As shown in Figure 1B, the red foci of **9** in FCCP-treated cells decrease significantly compared with the control, indicating that MMP is a critical factor. Moreover, to understand whether **9** entered mitochondria via the mitochondrial permeability transition pore (mPTP), the mPTP was blocked with cyclosporin (CsA), a potent mPTP inhibitor,[50] before the cells being treated with **9**. The results shown in Figure 1B indicate no significant change for the red foci compared to the control. Taken together, the results support that the delivery of **9** into mitochondria is mainly driven by MMP but not mPTP.

To confirm the substrates in mitochondria interacted with **9** is DNA but not RNA, enzymatic digestion assays were performed. From Figure 1C, the cells after DNase I treatment, the red foci were found almost completely disappeared; however, the red foci remained no obvious change after RNase A treatment. These results indicate that **9** binds to mtDNA in mitochondria. To further understand whether the mtDNA interacted with **9** in cells is G4 in nature, a reported G4-mtDNA binding ligand, MitoPDS,[23] was utilized for intracellular competition with **9** in living cells. From Figure 1D, the cells after being treated with MitoPDS, the red foci (ligand **9**) were found significantly decreased in a concentration-dependent manner. The results suggest that **9** and MitoPDS may compete with the same substrates in the cells and these substrates are presumably G4-mtDNAs.

It was previously reported that the upregulation of glycolysis by hypoxia could stimulate the formation of G4-mtDNA in cancer cells.[23] We thus use DMOG, a HIF-PH inhibitor,[51] that can upregulate glycolysis to treat HCT116 cells. The treated cells were then incubated with **9**. We found that the number of red foci (ligand **9**) in DMOG treated cells were increased significantly compared with the control (Figure 2A). On the contrary, for the treatment with HIF-1α inhibitors, 2MeOE2 and

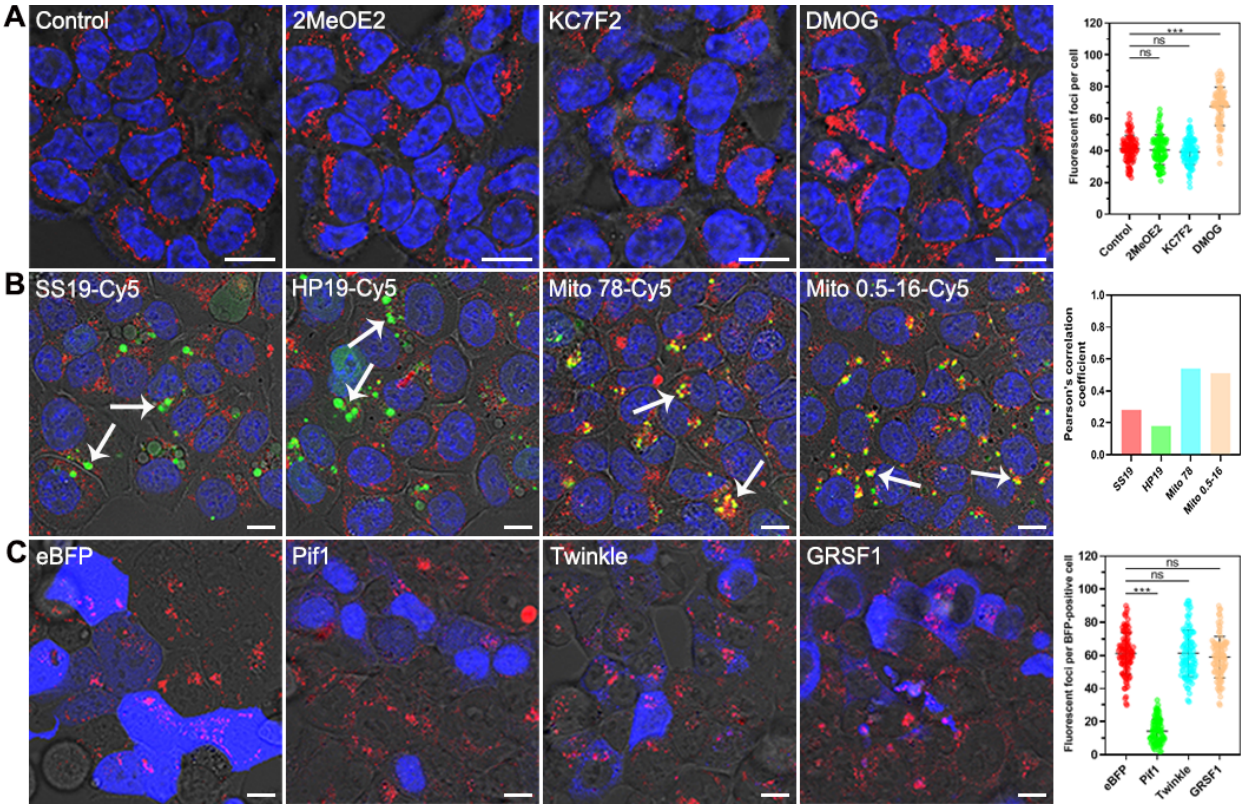

Figure 2. (A) Single confocal plane images: Living HCT116 cells incubated with 4 μM ligand **9** (λ_{ex}=488 nm) for 1 h and 1 μM Hoechst33342 (λ_{ex}=405 nm) for 30 min after treating 0.1 μM 2-MeOE2, 10 μM KC7F2, or 100 μM DMOG for 24 h. The scale bar is 10 μm. The image magnification is 400x. (B) Single confocal plane images for the co-localization analysis. Living HCT116 cells were transfected with Cy5-coupled mtDNA (λ_{ex}=635 nm) for 24 h and then incubated with 4 μM ligand **9** (λ_{ex}=488 nm) 1 h and 1 μM Hoechst33342 (λ_{ex}=405 nm) for 30 min. For the ease of visualization and comparison, pseudo-color (green) was used for the Cy5 label. The scale bar is 10 μm. The image magnification is 400x. (C) Single confocal plane images: Living HCT116 cells with overexpression of eBFP-tagged proteins (λ_{ex}=405 nm) and then incubated with 4 μM ligand **9** (λ_{ex}=488 nm) for 1 h. The scale bar is 10 μm. The image magnification is 400x. The data are presented as mean ± SEM, and statistical significance is determined by the t test as (ns) not significant, (*) $p < 0.05$, (**) $p < 0.01$, and (***) $p < 0.001$. 100 cells were measured.

KC7F2[52, 53] that can downregulate glycolysis, it only shows very little changes in the number of red foci in the cells compared with the control.

Moreover, the Cy5 coupled mitochondrial DNA was transfected into HCT116 cells. Our results showed that the transfected sequences were found both in cytoplasm and mitochondria (Figure S13A,B). Besides, the co-localization experiments for Cy5-G4-mtDNAs (*Mito 78* and *Mito 0.5-16*) and G4-specific antibody BG4 indicated that most transfected *Mito 0.5-16*-Cy5 and *Mito 78*-Cy5 could form G4-structures in HCT116 cells (Figure S13C,D). From Figure 2B, ligand **9** was found well co-localized with two Cy5-G4-mtDNAs (*Mito 78*: r = 0.54 and *Mito 0.5-16*: r = 0.51), but it was

poorly co-localized with Cy5-non-G4-DNAs (*SS19*: r = 0.28 and *HP19*: r = 0.18). Taken together, all these intracellular results further suggest that **9** may be able to target G4-mtDNAs in mitochondria of living HCT116 cells, although it is currently unclear which G4-mtDNA targets are bound with the ligand in the cells.

To obtain more information about the interaction of **9** with G4-mtDNA targets in living HCT116 cells, we overexpressed a G4-DNA-resolving helicase, Pif1, to unfold the G4s formed in mitochondria.[54] After overexpression of eBFP-tagged Pif1 in HCT116 cells, the red foci (ligand **9**) decreased significantly, while the negative control that only overexpressed eBFP showed no significant changes on the red foci (Figure 2C). Moreover, two non-G4-DNA-targeting helicases, Twinkle (a mtDNA helicase) and GRSF1 (a G4-mtRNA helicase),[55, 56] were overexpressed in HCT116 cells. Both Twinkle and GRSF1 are not able to unwind G4-DNA structures. As expected, these helicases showed no significant changes on the red foci (**9**) in mitochondria of living HCT116 cells (Figure 2C). Taken together, these intracellular results demonstrated with target-specific helicases further suggest that **9** may target G4-mtDNAs in mitochondria in living HCT116 cells.

2.4 The Effect of Ligand 9 in Inhibiting Replication, Transcription and Translation of Mitochondrial Genes in HCT116 Cells.

Mitochondria have their own DNA (mtDNA) to regulate the replication, transcription, and translation processes for maintaining proper functions to support various cellular activities. In these processes, G4s may play important roles in regulating the mitochondrial transcription and replication.[25] Ligand **9** is mitochondria-selective and also has high affinity binding to a number of G4-mtDNA targets examined. We thus investigated the effect of **9** on mitochondrial DNA replication, transcription and translation in HCT116 cells. As shown in Figure S14, the ligand showed inhibitory effects on mtDNA replication processes as indicated by a significant reduction in the copy numbers of ND1 and ND2 genes in HCT116 cells. It is noteworthy that this effect is not obvious in noncancerous HFF1 cells, implying that G4s may take regulatory roles in the replication process in HCT116 cancer cells.

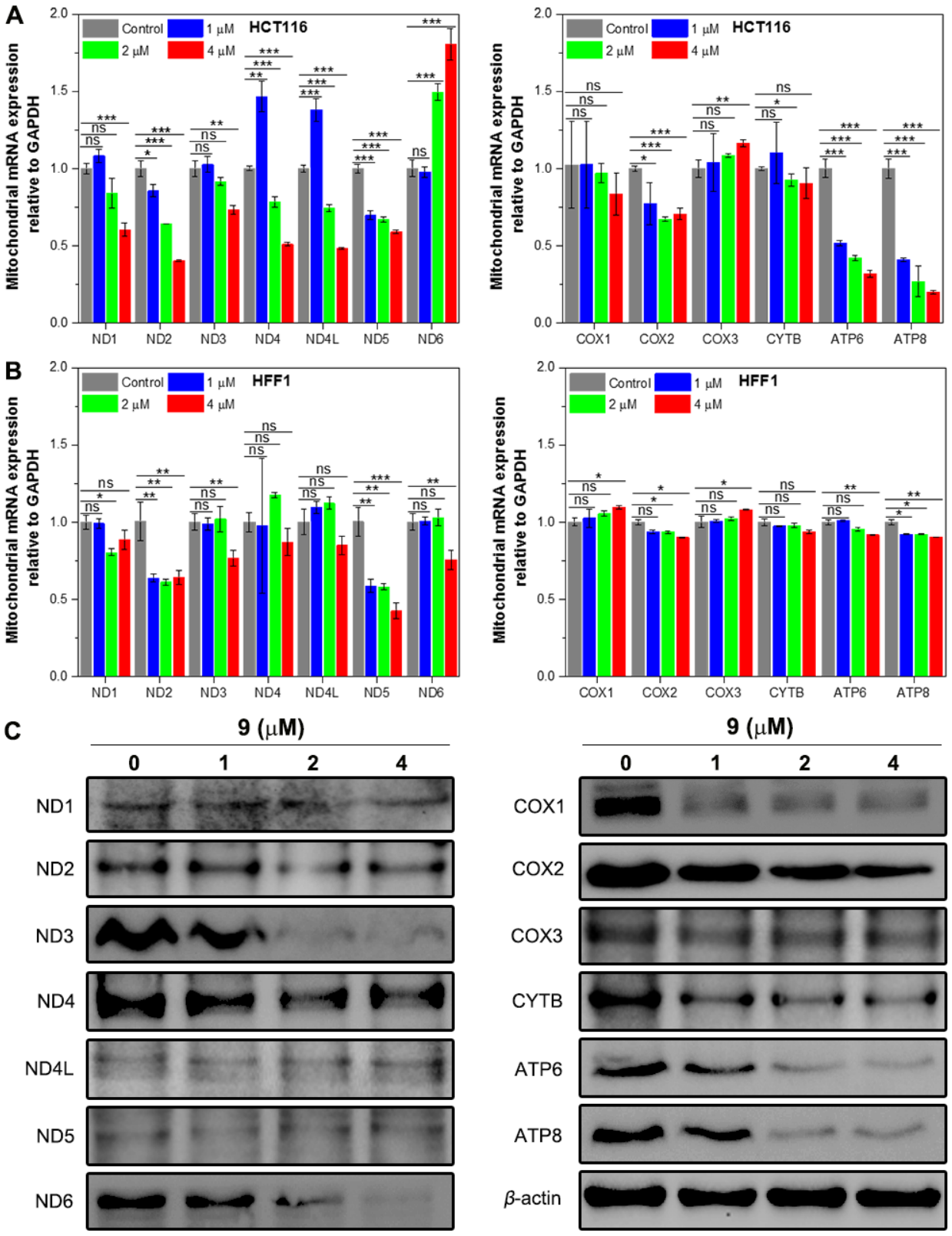

Figure 3. qRT-PCR study for the transcription and translation effects of **9**. (A) The influence of **9** (0-4 μM) on the transcription of the selected mitochondrial genes in HCT116 cells (cancer cell line). The incubation time was 48 h. (B) qRT-PCR study for the influence of **9** (0-4 μM) on the transcription of the selected mitochondrial genes in HFF1 cells (normal cell line). The incubation time was 48 h. The data are presented as mean ± SEM, and statistical significance is determined by the t test as (ns) not significant, (*) $p < 0.05$, (**) $p < 0.01$, and (***) $p < 0.001$. (C) Western blot assays to determine the protein expression level of ND1, ND2, ND3, ND4, ND4L, ND5, ND6, COX1, COX2, COX3, CYTB, ATP6, ATP8 and *β*-actin in HCT116 cells treated with **9** (0-4 μM) for 48 h.

To understand the effect of **9** on the transcription of mitochondrial genes, we investigated 13 important mitochondrial genes relevant to oxidative phosphorylation with real-time quantitative reverse transcription PCR (qRT-PCR) in both HCT116 cells and HFF1 cells. The results indicate that HCT116 and HFF1 cells treated with **9** show markedly different transcriptional activity (Figure 3A,B). In HCT116 cells, **9** caused a significant reduction of mRNA levels for ND1, ND2, ND3, ND4, ND4L, ND5, COX2, ATP6 and ATP8. Interestingly, the effect of **9** in HFF1 cells was found markedly different from HCT116 cells because only ND2 and ND5 showed a significant reduction. Moreover, Western blotting assays showed that the protein levels of ND3, ND4, ND6, COX1, COX2, COX3, CYTB, ATP6 and ATP8 were decreased markedly in the HCT116 cells treated with **9** (Figure 3C). Furthermore, since these 13 mitochondrial genes are subunits of the five complexes that make up the mitochondrial respiratory chain, ligand **9** may also cause the downregulation of these complexes. As expected, Western blotting results showed evidently that the level of complex I, II, III and IV were downregulated markedly in the **9**-treated HCT116 cells (Figure S15). Collectively, ligand **9** selectively binds to G4-mtDNA targets with high affinity in mitochondria and effectively inhibits the replication, transcription and translation of mtDNA in HCT116 cells.

2.5 The Effect of Ligand 9 in Causing Mitochondrial Dysfunction.

To understand whether **9** interrupted mitochondrial functions, we studied MMP changes of HCT116 cells treated with the ligand. As shown in Figure 4A, the **9**-treated cells were stained with a TMRE dye (tetramethylrhodamine ethyl ester) and the intensitiy of TMRE-staining in the cells was found clearly decreased with **9** treatment in a concentration dependent manner. The reduced TMRE-staining indicates the decrease of MMP. It is probably attributed to the depolarization of MMP by **9** because this ligand is di-cationic. Then, the reactive oxygen species (ROS) production in HCT116 cells treated with **9** was studied with a mitochondrial ROS probe MitoSOX. We found that **9** upregulated the ROS level in a concentration dependent manner (Figure 4B). The increased ROS level may cause DNA damage in cells. Taken together, these results suggest that **9** may downregulate the expression level of five complexes of the mitochondrial respiratory chain and cause mitochondrial dysfunction.

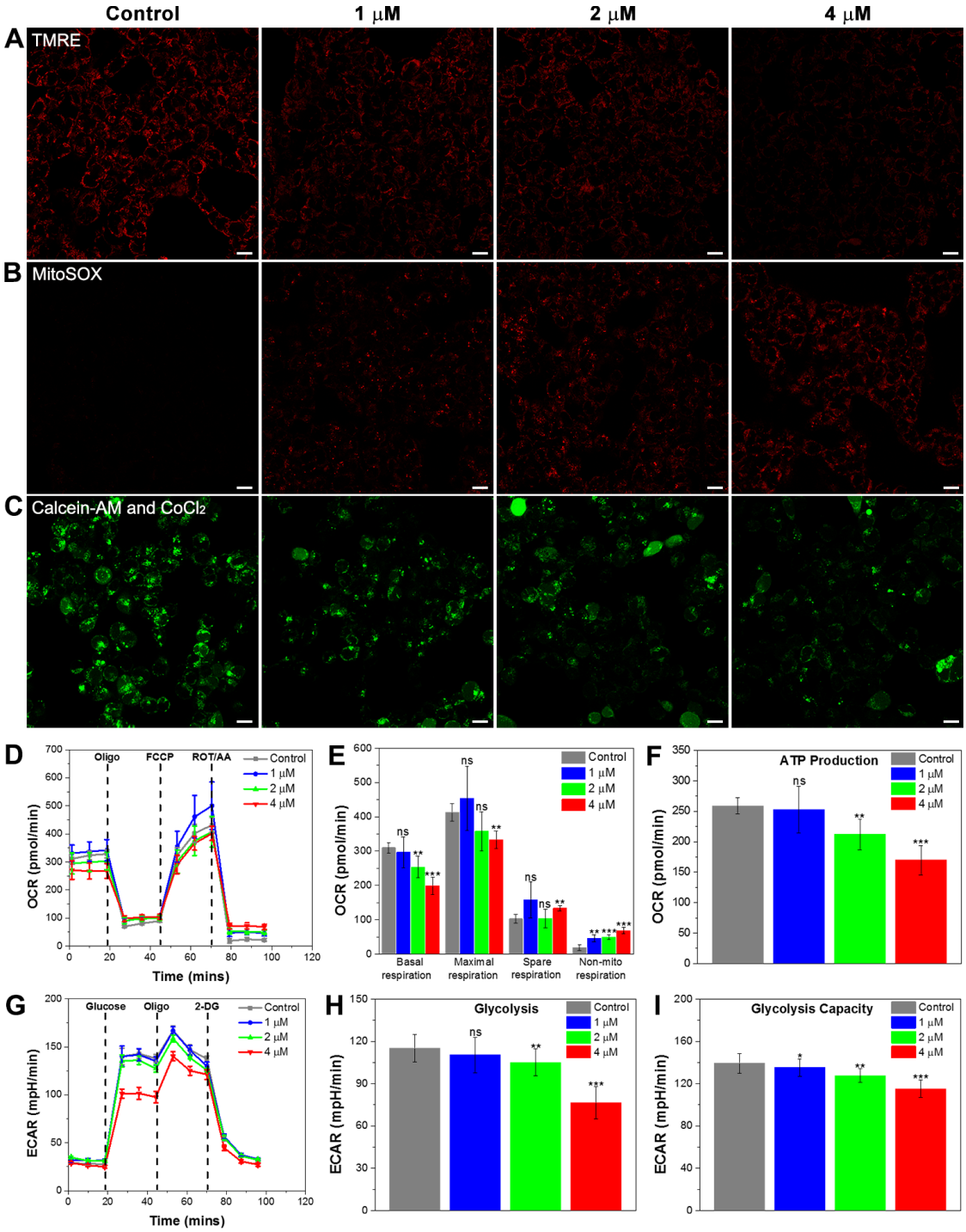

Figure 4. (A) Single confocal plane images: The effect of **9** (0-4 μM) on MMP in HCT116 cells. MMP was evalulated with TMRE (λ_{ex}=561 nm); incubation for 48 h. The scale bar is 10 μm. The image magnification is 400x. (B) Single confocal plane images: Ligand **9** (0-4 μM) induces ROS production in HCT116 cells and ROS was stained with MitoSOX (λ_{ex}=405 nm); incubation for 48 h. The scale bar is 10 μm. The image magnification is 400x. (C) Single confocal plane images: The effect of **9** (0-4 μM) on mPTP opening in HCT116 cells. The mPTP opening was evaluated with Calcein-AM (λ_{ex}=488 nm) and $CoCl_2$ assays; incubation for 48 h. The scale bar is 10 μm. The image magnification is 400x. (D) Seahorse experiments to study OCR of HCT116 cells treated with **9** (0-4 μM) for 3 h in response to electron transfer chain inhibitors (n=5). (E) Values of the basal respiration, maximal respiration, spare respiratory and non-mitochondrial respiration capacity. (F) The analysis of ATP production of **9**-treated cells. (G) Seahorse experiments to study ECAR of HCT116 cells treated with **9** (0-4 μM) for 3 h in response to glucose stimulation (n=5). (H) Changes of glycolysis. (I) Changes of glycolysis capacity. The data are presented as mean ± SEM, and statistical significance is determined by the t test as (ns) not significant, (*) $p < 0.05$, (**) $p < 0.01$, and (***) $p < 0.001$.

Moreover, **9** promoted the opening of mPTP in HCT116 cells in a dose-dependent manner (Figure 4C). This effect may further promote the delivery of **9** into mitochondria.

To further verify the effect of **9** in the induction of mitochondrial dysfunction in HCT116 cells, we conducted Mito-stress test and glycolysis stress test for the cells treated with the ligand. The oxygen consumption rate (OCR) and extracellular acidification rate (ECRA) were determined for the HCT116 cells treated with the ligand for 3 h. The results showed that OCR, ECRA, ATP production, and glycolysis were significantly decreased (Figure 4D-I). These results evidently support that **9** reduces oxidative phosphorylation and glycolysis in HCT116 cells. Subsequently, the ability of the cells in energy production may be inhibited due to the significantly reduced mitochondrial performance. Eventually, it may cause cellular senescence.

2.6 The Effect of Ligand 9 in Inducing DNA Damage and Cellular Senescence.

We found that **9** induced a markedly increase in mitochondrial ROS level in HCT116 cells. Thus, we investigated whether the ligand could cause DNA damage. The results of Comet assays reveal that **9** may cause DNA damage, as indicated by the lengthened comet tails observed in HCT116 cells treated with the ligand (Figure 5A and Figure S16C). Besides, the significantly increased γ-H2AX protein level also evidently reveals that **9** induces DNA damage in HCT116 cells (Figure 5G). To further prove that the mtROS production induced by **9** is a major cause of DNA damage, we used MitoTEMPOL, a mitochondria-targeted antioxidant, to reduce the mtROS level in HCT116 cells treated with **9**. As shown in Figure S16A, the ROS induced by **9** was inhibited significantly in the presence of MitoTEMPOL as expected. Besides, Comet assay (Figure S16B) showed that DNA damage caused by **9** was also inhibited in HCT116 cells treated with MitoTEMPOL because the tail moment length was significantly reduced (Figure S16C). Moreover, the cells after being treated with MitoTEMPOL, the DNA damage marker γ-H2A.x was downregulated (Figure S16D). Therefore, the mtROS induced by **9** may be the major trigger of DNA damage in HCT116 cells.

Cellular senescence is a state of stable cell cycle arrest under which cells remain metabolically active, but no longer divide and do not respond to growth-promoting stimuli.[57-59] Senescence can be

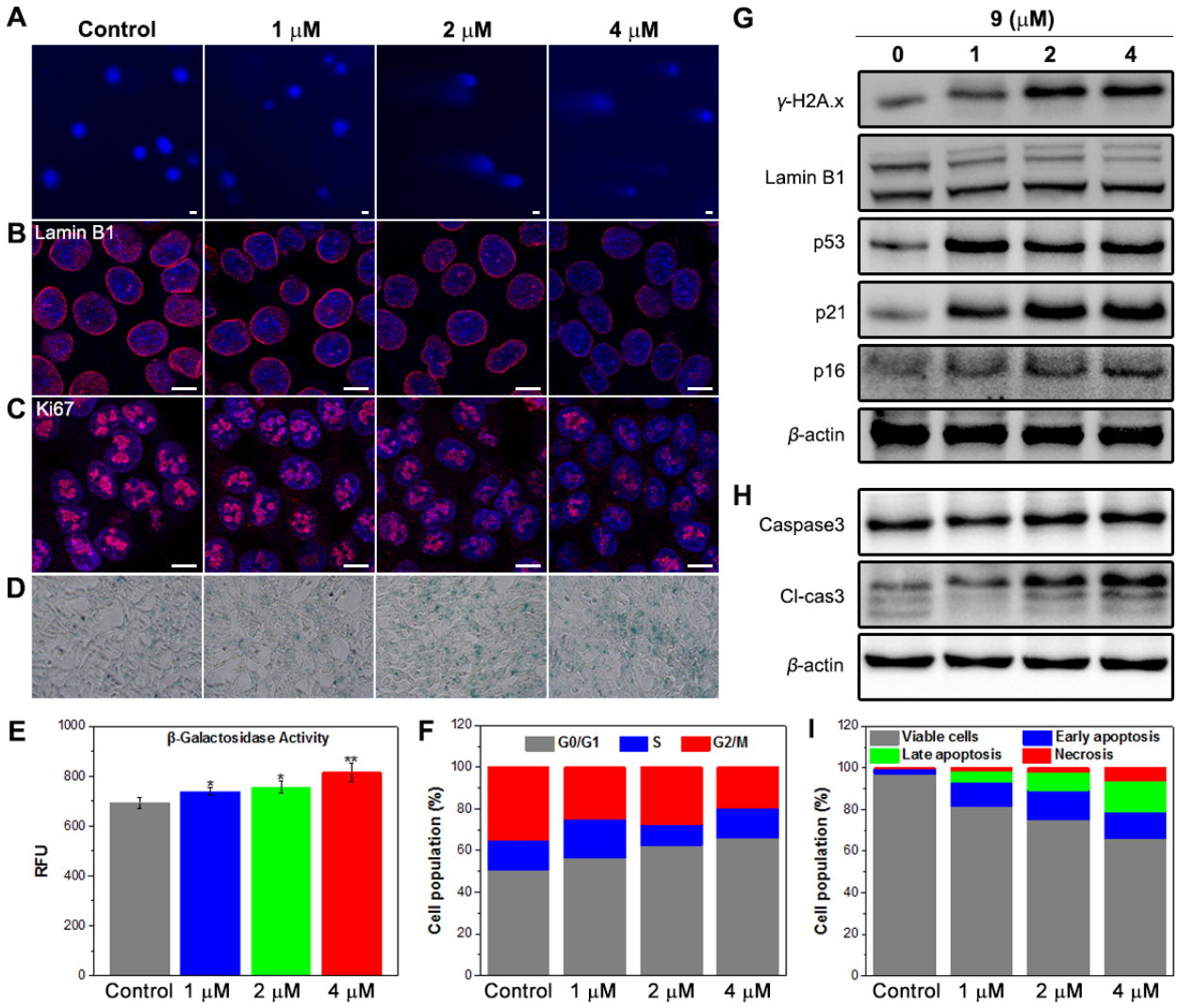

Figure 5. (A) Comet assay to analyze DNA damage induced by **9** (0-4 μM) for 72 h treatment in the cells. The cell was stained by DAPI (λ_{ex}=405 nm). The scale bar is 10 μm. The image magnification is 200x. The lengthened comet tail image indicates DNA damage. (B) Immunofluorescence analysis of Lamin B1 (λ_{ex}=635 nm) in HCT116 cells after **9** (0-4 μM) treatment for 72 h. The scale bar is 10 μm. The image magnification is 400x. (C) Immunofluorescence analysis of Ki67 (λ_{ex}=635 nm) in HCT116 cells after **9** (0-4 μM) treatment for 72 h. The scale bar is 10 μm. The image magnification is 400x. (D) SA-*β*-gal assay was used to detect the senescence of HCT116 cells after **9** (0-4 μM) treatment for 72 h. The image magnification is 100x. (E) *β*-galactosidase activity of HCT116 cells after **9** (0-4 μM) treatment for 72 h. The data are presented as mean ± SEM, and statistical significance is determined by the t test as (ns) not significant, (*) $p < 0.05$, (**) $p < 0.01$, and (***) $p < 0.001$. (F) Cell cycle analysis of HCT116 cells treated with **9** (0-4 μM) for 72 h. (G) Western blot assays to determine the translation of Lamin B1, p53, p21, p16, *γ*-H2A.x, and *β*-actin in HCT116 cells treated with **9** (0-4 μM) for 72 h. (H) Western blot assays to determine the translation of Caspase3, Cleaved-caspase3 and *β*-actin in HCT116 cells after **9** (0-4 μM) treatment for 72 h. (I) Cell apoptosis analysis of HCT116 cells treated with **9** (0-4 μM) for 72 h. The cells were stained by Annexin V-BUV396 and 7-AAD.

triggered by various factors including oxidative stress, DNA damage, and mitochondrial dysfunction.[57-59] The cellular results clearly show that **9** causes mitochondrial dysfunction, increases ROS production, and induces DNA damage in HCT116 cells. We therefore speculate that **9** may also

induce cellular senescence. Lamin B1 is a known nuclear membrane structural component. The downregulation of Lamin B1 represents an established biomarker for cellular senescence.[60] The immunofluorescence and Western blotting results show that the protein level of Lamin B1 decreases markedly in the HCT116 cells treated with **9** in a concentration-dependant manner (Figure 5B,G). Also, the cell proliferation marker Ki67 was found clearly decreased in the cells treated with **9** (Figure 5C), suggesting that **9** inhibited the growth of HCT116 cells. Furthermore, **9** was applied in SA-*β*-gal assays to study its effect on senescence of HCT116 cells. As shown in Figure 5D, it is obvious that **9** is positive in the SA-*β*-gal staining. Besides, the *β*-galactosidase activity of HCT116 cells was found to increase by 6.61%-17.63% after the treatment with **9** (Figure 5E), suggesting that about 17.63% cells were senescent finally.

The results of cell cycle analysis indicated that the HCT116 cells treated with **9** were arrested in G0/G1 phase. The percentage of G0/G1 phase is increased from 50.66% to 66.01%, in a concentration-dependent manner (Figure 5F and Figure S17). Moreover, p53, p21 and p16, the inhibitors of cell cycle, were also found upregulated for the cells treated with **9** (Figure 5G). The apoptosis marker cleaved-caspase3 was also increased markedly in the **9**-treated HCT116 cells (Figure 5H). By staining the HCT116 cells with Annexin V-BUV396 and 7-AAD, **9** induces apoptosis in a dose-dependent manner, and it is increased from 2.64% to 27.4% (Figure 5I and Figure S18). Taken together, these results suggest that **9** causes substantial mitochondrial dysfunction and DNA damage in HCT116 cells, and eventually it induces senescence and apoptosis.

2.7 RNA-sequencing Analysis Indicating Ligand 9 Targeting Mitochondria in HCT116 Cells.

To get more information on cellular targets of **9** in HCT116 cells, we performed RNA-sequencing for the cells treated with **9** at 4 μM. DMSO was used as a control. Heatmap and vocano plot showed an overview of the differentially expressed genes (Figures 6A and Figure S19). Only about 3% of the total genes were influenced by **9** (0.8% genes were upregulated and 2.2% genes were downregulated with log2 fold change > 1 or < -1 and padj < 0.05). These results suggest that the targets of **9** in HCT116 cells are relatively concentrated and thus a low off-target effect could be expected. Of these

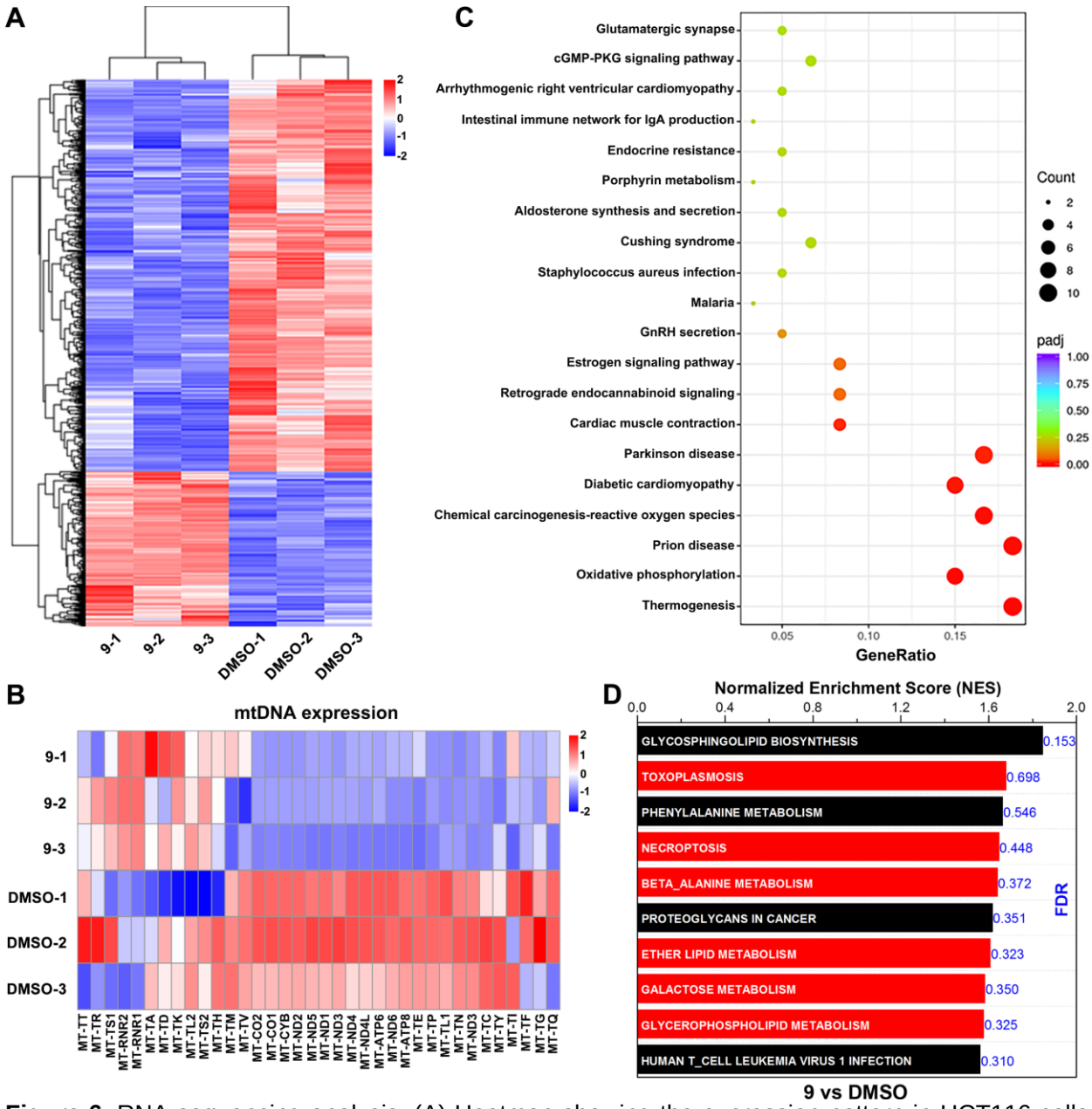

Figure 6. RNA-sequencing analysis. (A) Heatmap showing the expression pattern in HCT116 cells treated with 4 μM ligand **9** (vs 0.08% DMSO). Genes are clustered using hierarchical clustering. Red indicates higher expression, and blue indicates lower expression. Color bar indicates row Z score. (B) Heatmap showing the effect of 4 μM ligand **9** on mtDNA expression after 48 h treatment as determined by RNA-Seq. (C) KEGG enrichment analysis of genes change after 4 μM ligand **9** treatment. The size of bubbles represents the number of genes in each term. (D) The top 10 significantly enriched pathways in HCT116 cells treated with 4 μM ligand **9** (*versus* 0.08% DMSO).

affected genes, 20 genes in the mitochondria were affected, of which 13 were downregulated and 7 upregulated with log2 fold change > 2 or < -2 and padj < 0.05 (Figure 6B). Interestingly, in the 13 genes related to the mitochondrial respiratory chain, most of them were downregulated. The finding is consistent with the results of qRT-PCR and Western blotting shown in Figure 3. Moreover, most of these downregulated genes contain G-rich sequences showing high propensity to form G4-

structures, which are the potential targets of **9**. The stabilization of these G4-mtDNA structures with **9** *in cellulo* may inhibit gene expression in both transcriptional and translational level.

For the enrichment and differential analysis, the Kyoto Encyclopedia of Genes and Genomes (KEGG) enrichment was showed in Figure 6C. Among the 20 most influenced KEGG enrichment pathways in RNA-seq, oxidative phosphorylation was influenced markedly (Figure S20). Additionally, the gene set enrichment analysis (GSEA) showed that 6 mitochondria-related pathways (red) were influenced by **9** in the top 10 markedly enriched pathways (Figure 6D), including toxoplasmosis, necroptosis, *β*-alanine metabolism, ether lipid metabolism, galactose metabolism and glycerophospholipid metabolism. These enriched pathways are found related to mitochondria. The ROS produced by mitochondria has an important relationship with toxoplasmosis and necroptosis,[61, 62] since **9** induces ROS production in mitochondria in HCT116 cells, and these two pathways may possibly be influenced. Moreover, ether lipid plays vital roles in mitochondria against oxidative stress.[63] The excess ROS in mitochondria induced by **9** may thus influence the ether lipid metabolism. In addition, *β*-alanine and galactose are directly related to oxidative phosphorylation.[64, 65] We have verified that **9** is able to downregulate the oxidative phosphorylation in HCT116 cells. Therefore, the metabolism of *β*-alanine and galactose may be influenced in the cells treated with **9**. Furthermore, mitochondria are the sites for the synthesis of some phospholipids including cardiolipin, phosphatidylglycerol and phosphatidylethanolamine.[66] The mitochondrial dysfunction caused by **9** may therefore affect the metabolism of glycerophospholipid. Collectively, RNA-seq analysis reveals that **9** is concentratedly targeting mitochondria in HCT116 cells.

2.8 Ligand 9 shows potent antitumor efficacy in a mouse xenograft model of colorectal cancer *in vitro* an *in vivo*.

To further evaluate the *in vitro* anticancer activity of **9** against colorectal cancer cells, we performed trans-well assays and colony formation assays to study the influence of **9** on morphology, migration and colony formation of HCT116 cells. As shown in Figure 7A, the morphology of HCT116 cells

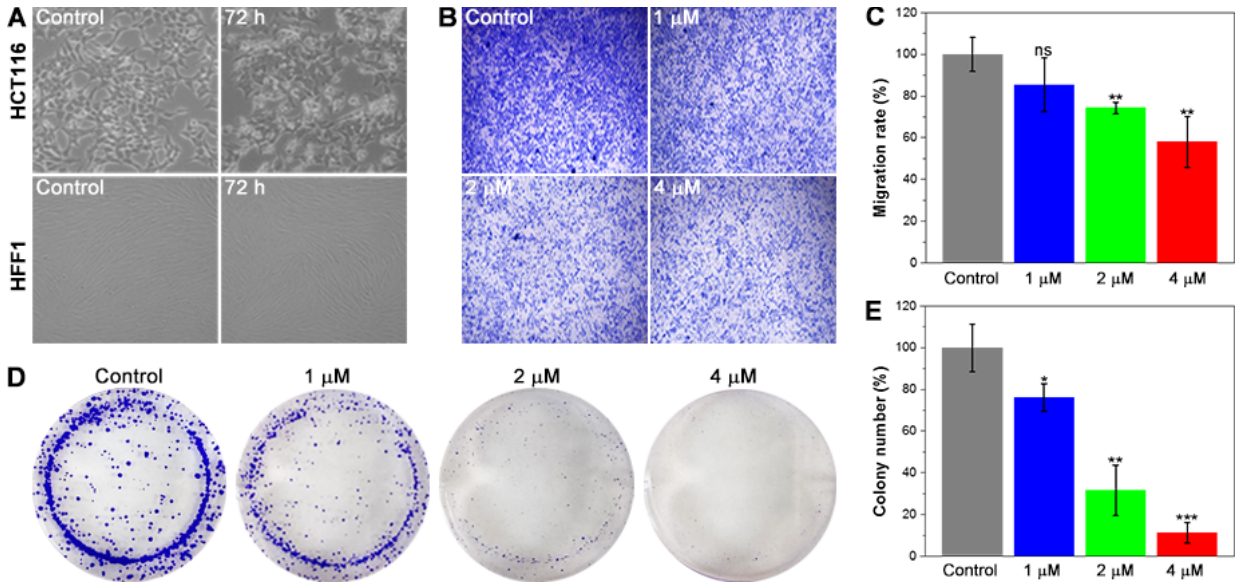

Figure 7. (A) The study of cell morphology for HCT116 and HFF1 cells treated with **9** (4 μM) and without **9** treatments (control). The image magnification is 100x. (B) The migration of HCT116 was treated with **9** for 72 h at a concentration of 0, 1, 2, 4 μM by Trans-well assay. The image magnification is 100x. (C) The quantification of the trans-well assay. Data are expressed as mean ± SD; **p* < 0.05, ***p* < 0.01, ****p* < 0.001. (D) The inhibition of cancer cell proliferation. HCT116 cells were treated with ligand **9** for 7 days at a concentration of 0, 1, 2, 4 μM, and their clone formation were determined. (E) The quantification of the colony-forming assay. Data are expressed as mean ± SD; **p* < 0.05, ***p* < 0.01, ****p* < 0.001.

and HFF1 cells after being treated with **9** at 4 μM was found clearly different. Obviously, **9** caused more cell death in HCT116 compared to HFF1 cells. The HCT116 cell migration was also inhibited by **9** with a reduction of 40% (Figure 7B,C). In addition, for the HCT116 cells treated with **9**, the proliferation ability was markedly decreased in a concentration-dependent manner (Figure 7D). The proliferation was almost completely suppressed by **9** at 4 μM (Figure 7E). All these results suggest that **9** shows potent anticancer activity against human colorectal cancer.

A xenograft mouse model of HCT116 was utilized to evaluate the *in vivo* antitumor efficacy of **9**. Two groups of HCT116 tumor-bearing male Balb/c nude mice (6 mice per group) were injected intravenously every two days (Group 1 (PBS) and Group 2 (**9**, 5 mg/kg)). The *in vivo* results show that the dose at 5 mg/kg did not influence the growth of mice because the body weight of mice in two groups did not show significant changes (Figure 8A). Nonetheless, **9** significantly inhibited the growth of tumors (Figure 8B-E). Compared to the control group, the tumor growth in terms of tumor weight for the **9**-treated group was reduced by 70% approximately. Moreover, the tumor tissues taken

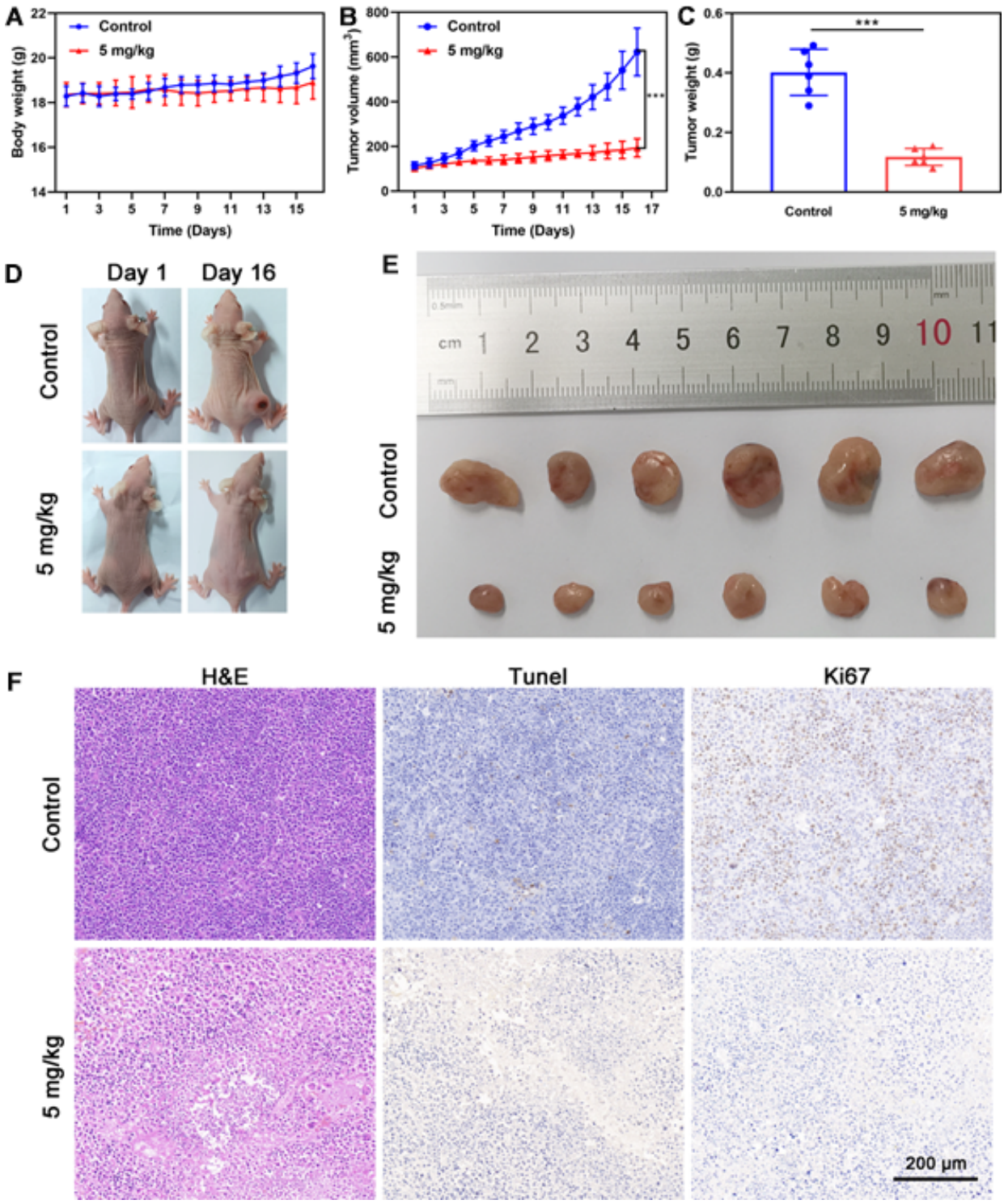

Figure 8. The evaluation of *in vivo* antitumor efficacy of **9**. (A) Body weight change of HCT116 tumor-bearing nude mice injected with **9** (5 mg/kg) in tail vein over 16 days (n=6, mean ± SD). (B) Time-dependent change of tumor volume after different treatments for 16 days (n=6, mean ± SD, *$p < 0.05$, **$p < 0.01$, and ***$p < 0.001$). (C) Weight of isolated tumors in HCT116 tumor-bearing nude mice after 16 days of treatment (n=6, mean ± SD, *$p < 0.05$, **$p < 0.01$, and ***$p < 0.001$). (D) Digital photographs of HCT116 tumor-bearing nude mice on day 1 and day 16 of different groups. (E) Digital photographs of isolated tumors from different groups of HCT116-bearing nude mice after 16 days. (F) Representative histological images of H&E, TUNEL and Ki67 antigen immunofluorescence-stained tumor tissue sections of HCT116 tumor-bearing nude mice tumors from different groups after 16 days of treatment. The scale bar is 200 μm. The image magnification is 200x.

from the mice were analyzed. The nuclear sequestration and fragmentation in H&E images were clearly observed compared to the control group. TUNEL staining data also showed that **9** promoted apoptosis of tumor cells. Furthermore, Ki67 staining assays showed clearly that **9** inhibited tumor cell proliferation (Figure 8F). Taken together, the *in vivo* results support that **9** shows high potency against human colorectal cancer.

To further evaluate the biocompatibility and *in vivo* toxicity of **9**, whole blood samples were collected for biochemical blood analysis when mice were killed on day 16. The biochemical parameters including white blood cell count, lymphocyte count, neutrophil count, red blood cell count, hemoglobin, mean red blood cell volume, mean red blood cell hemoglobin content, mean red blood cell hemoglobin concentration, mean platelet volume, and platelet count were analyzed. The results were shown in Figure S21A, compared with the control group, there was no significant change in all biochemical parameters for the mice treated with **9**. More importantly, the H&E staining sections of major organs of the mice including heart, liver, spleen, lung and kidney, support that **9** may have low or no observable toxic effects to these organs (Figure S21B). Therefore, **9** shows high potential to be a new and potent anti-colorectal cancer agent that may target both mitochondria and the G4-mtDNA structures with low *in vivo* cytotoxicity.

3. CONCLUSIONS

In conclusion, a new small-sized di-cationic ligand **9** tailored with the functionality of mitochondria-selective and G4-mtDNA-targeting was developed and demonstrated in living human colorectal cancer cells (HCT116). The affinity of the ligand binding to G4-mtDNA targets *in vitro* determined with SPR and ITC is strong and down to nanomolar level. In addition, the ligand exhibits potent anticancer activity against HCT116 cancer cells, while it has a markedly less cytotoxic against noncancerous human cells. The results of qRT-PCR and Western blotting show that the ligand downregulates markedly the expression of most mitochondrial respiratory chain related genes including ND3, ND4, ND6, COX1, COX2, COX3, CYTB, ATP6 and ATP8, and also inhibits the

expression of the respiratory chain complexes I-IV. Furthermore, the ligand causes substantial mitochondrial dysfunction including depolarizing mitochondrial membrane potential, inducing ROS production and mPTP opening, and downregulating both the oxidative phosphorylation and glycolysis. More importantly, the ligand induces DNA damage, senescence and apoptosis in HCT116 cancer cells. The trans-well assay and colony formation assay also show that the ligand is able to inhibit the migration and proliferation of HCT116 cells. The *in vivo* antitumor efficacy of the ligand against human colorectal cancer xenografts (HCT116) in nude mice was validated. The ligand at 5 mg/kg was able to reduce the tumor weight by 70% compared to the control. Taken together, the di-catioinic ligand is a novel mitochondria-selective and G4-mtDNA-targeting anticancer agent for human colorectal cancer therapy with high potency and low toxicity.

4. EXPERIMENTAL SECTION

4.1 Synthesis and Characterization.

High resolution mass spectra (HRMS) were obtained by Agilent 1260-6230TOF. By use of TMS as a reference, ^{1}H and ^{13}C NMR spectra were recorded at 400 and 100 MHz in DMSO-d_6 with a Bruker BioSpin GmbH spectrometer. The high-performance liquid chromatography (HPLC) analysis for examining the purity of the ligands was performed on a SHIMADZU LC-16 system using a Diamonsil C18 column (250 mm × 4.6 mm, 5 μm) at room temperature with an elution using the mobile phase (MeOH/H_2O = 50:50, v/v). All ligands synthesized for assays were confirmed to have a purity ≥ 95%.

General Procedures for the Synthesis of ligands (**1−10**). A synthetic route to ligands **1–10** is shown in **Scheme 1**. Intermediate **a** was obtained by the reaction using 2-methylquinoline (1.002 g, 7.0 mmol) and 1, 8-diiodooctane (1.244 g, 3.4 mmol) in ethanol (10 mL) under 100 °C for 24 h. Recrystallization of the crude product with acetone to obtain brown-green solid in 73% yield. Ligands **1–10** were obtained by the reaction of intermediate **a** (0.1 g, 0.15 mmol) and benzaldehyde (0.042 g, 0.4 mmol), p-methyl benzaldehyde (0.048 g, 0.4 mmol), 4-(dimethylamino)benzaldehyde (0.059 g, 0.4 mmol),

Indole-3-carboxaldehyde (0.058g, 0.4 mmol), 1H-indole-2-carbaldehyde (0.058 g, 0.4 mmol), 4-(methylthio)benzaldehyde (0.061 g, 0.4 mmol), N-ethylcarbazole-3-carboxaldehyde (0.089 g, 0.4 mmol), 4-(1-pyrrolidino)benzaldehyde (0.070 g, 0.4 mmol), 4-(piperidin-1-yl)benzaldehyde (0.076 g, 0.4 mmol) or 4-morpholinobenzaldehyde (0.076 g, 0.4 mmol) and 4-methylpiperidine (30 μL), ethanol (3 mL) in 100 °C refluxed overnight. The crude products were purified by flash silica gel column chromatography (MeOH/DCM = 1:20, v/v). The pure ligands obtained were characterized by ^{1}H NMR, ^{13}C NMR, and HRMS. The purity of ligands determined with HPLC analysis was ≥ 95%.

A synthetic route to the ligands **11** and **12** is shown in **Scheme S1**. Intermediate **b** and **c** were obtained by the reaction using 2-methylquinoline (0.286 g, 2.0 mmol) and Iodomethane (0.426 g, 3.0 mmol) or 1-iodobutane (0.552 g, 3.0 mmol) in acetonitrile (4 mL) under 80 °C overnight. Ligands **11** and **12** were obtained by the reaction of intermediate **b** (0.142 g, 0.5 mmol) or intermediate **c** (0.164 g, 0.5 mmol) with 4-(Piperidin-1-yl)benzaldehyde (0.132 g, 0.7 mmol), and 4-methylpiperidine (30 μL), ethanol (3 mL) in 100 °C refluxed overnight. The crude products were purified by flash silica gel column chromatography (MeOH/DCM = 1:20, v/v). The pure ligands obtained were characterized by ^{1}H NMR, ^{13}C NMR, and HRMS. The purity of ligands determined with HPLC analysis was ≥ 95%.

*(E)-1,1'-(octane-1,8-diyl)bis(2-((E)-styryl)quinolin-1-ium) iodide (**1**).* Brown solid with 65% yield. ^{1}H NMR (400 MHz, DMSO-d_6) δ 9.14 (d, J = 8.9 Hz, 2H), 8.61 (d, J = 9.0 Hz, 2H), 8.55 (d, J = 9.1 Hz, 2H), 8.41 (d, J = 7.1 Hz, 2H), 8.25 – 8.17 (m, 4H), 7.99 (t, J = 7.6 Hz, 2H), 7.97 – 7.91 (m, 4H), 7.88 (d, J = 15.9 Hz, 2H), 7.49 (d, J = 7.3 Hz, 6H), 5.19 – 5.06 (m, 4H), 1.86 (m, 4H), 1.51 (m, 4H), 1.35 (m, 4H). ^{13}C NMR (100 MHz, DMSO-d_6) δ 156.06, 147.77, 145.26, 138.71, 135.79, 135.26, 131.84, 130.98, 129.61, 128.84, 122.09, 119.62, 119.32, 51.16, 29.02, 26.11. HRMS m/z: calcd for $C_{42}H_{42}N_2^{2+}$, $[M]^{2+}$ = 287.3976, found 287.1637. HPLC analysis: retention time at 5.141 min eluted with MeOH/H_2O = 50:50 (v/v), purity = 99.1%.

*(E)-1,1'-(octane-1,8-diyl)bis(2-((E)-4-methylstyryl)quinolin-1-ium) iodide (**2**).* Brown solid with 68% yield. ^{1}H NMR (400 MHz, DMSO-d_6) δ 9.10 (d, J = 8.9 Hz, 2H), 8.57 (d, J = 8.7 Hz, 2H), 8.52 (d, J = 9.0 Hz, 2H), 8.39 (d, J = 8.1 Hz, 2H), 8.15 (d, J = 15.7 Hz, 4H), 7.98 (d, J = 7.1 Hz, 2H), 7.80 (t, J = 11.0 Hz, 6H), 7.24 (d, J = 7.9 Hz, 4H), 5.06 (m, 4H), 2.24 (s, 6H), 1.77 (m, 4H), 1.52 (m, 4H), 1.36 (m, 4H). ^{13}C NMR (100 MHz, DMSO-d_6) δ 156.07, 147.98, 144.98, 142.24, 138.67, 135.68, 132.61, 130.96, 130.18, 129.61, 128.69, 121.90, 119.52, 118.12, 50.88, 28.96, 28.68, 25.92, 21.55. HRMS m/z: calcd for $C_{44}H_{46}N_2^{2+}$, $[M]^{2+}$ = 301.4242, found 301.1835. HPLC analysis: retention time at 5.141 min eluted with MeOH/H_2O = 50:50 (v/v), purity = 99.1%.

*(E)-1,1'-(octane-1,8-diyl)bis(2-((E)-4-(dimethylamino)styryl)quinolin-1-ium) iodide (**3**).* Dark green solid with 61% yield. ^{1}H NMR (400 MHz, DMSO-d_6) δ 8.77 (d, J = 9.1 Hz, 2H), 8.42 (d, J = 9.2 Hz, 2H), 8.37 (d, J = 8.8 Hz, 2H), 8.25 (d, J = 7.0 Hz, 2H), 8.14 (d, J = 15.1 Hz, 2H), 8.07 (t, J = 7.8 Hz, 2H), 7.85 (t, J = 7.6 Hz, 2H), 7.72 (d, J = 8.9 Hz, 4H), 7.33 (d, J = 15.5 Hz, 2H), 6.64 (d, J = 9.0 Hz, 4H), 4.90 (m, 4H), 2.88 (s, 12H), 1.84 (m, 4H), 1.61 (m, 4H), 1.46 (m, 4H). ^{13}C NMR (100 MHz, DMSO-d_6) δ 155.80, 153.05, 149.76, 142.56, 138.62, 134.84, 132.32, 130.58, 128.55, 127.57, 122.67, 120.76, 118.92, 112.15, 111.23, 49.85, 28.47, 25.76. HRMS m/z: calcd for $C_{46}H_{52}N_4^{2+}$, $[M]^{2+}$ = 330.4654, found 330.2107. HPLC analysis: retention time at 5.124 min eluted with MeOH/H_2O = 50:50 (v/v), purity = 98.5%.

*(E)-1,1'-(octane-1,8-diyl)bis(2-((E)-2-(1H-indol-3-yl)vinyl)quinolin-1-ium) iodide (**4**).* Orange solid with 71% yield. ^{1}H NMR (400 MHz, DMSO-d_6) δ 12.29 (s, 2H), 8.82 (d, J = 9.2 Hz, 2H), 8.62 (d, J = 15.3 Hz, 2H), 8.56 (d, J = 9.3 Hz, 2H), 8.38 (d, J = 9.0 Hz, 2H), 8.32 (s, 2H), 8.26 (d, J = 7.0 Hz, 2H), 8.07 (dd, J = 7.8, 3.5 Hz, 4H), 7.84 (t, J = 7.5 Hz, 2H), 7.49 – 7.45 (m, 2H), 7.40 (d, J = 15.4 Hz, 2H), 7.23 – 7.18 (m, 4H), 4.97 – 4.87 (m, 4H), 1.89 (m, 4H), 1.63 (m, 4H), 1.48 (m, 4H). ^{13}C NMR (100 MHz, DMSO-d_6) δ 185.43, 156.26, 143.95, 142.52, 138.93, 138.65, 138.12, 137.51, 135.64, 134.81, 130.62, 128.45, 127.41, 125.41, 123.92, 122.58, 122.35, 121.28, 120.44, 118.75, 118.62 – 118.53, 114.97, 113.47, 112.89, 111.08, 50.17, 29.08, 28.43, 26.35. HRMS m/z: calcd for

$C_{46}H_{44}N_4^{2+}$, $[M]^{2+}$ = 326.4336, found 326.1794. HPLC analysis: retention time at 5.121 min eluted with MeOH/H_2O = 50:50 (v/v), purity = 98.1%.

*(E)-1,1'-(octane-1,8-diyl)bis(2-((E)-2-(1H-indol-2-yl)vinyl)quinolin-1-ium) iodide (**5**).* Orange solid with 66% yield. ^{1}H NMR (400 MHz, DMSO-d_6) δ 11.90 (s, 2H), 8.97 (d, *J* = 9.0 Hz, 2H), 8.51 (d, *J* = 9.1 Hz, 2H), 8.40 (d, *J* = 9.1 Hz, 2H), 8.33 (d, *J* = 7.1 Hz, 2H), 8.23 (d, *J* = 15.6 Hz, 2H), 8.13 (t, *J* = 7.4 Hz, 2H), 7.92 (t, *J* = 7.5 Hz, 2H), 7.64 (d, *J* = 15.7 Hz, 2H), 7.53 (d, *J* = 8.0 Hz, 2H), 7.38 (d, *J* = 8.2 Hz, 2H), 7.13 (t, *J* = 7.6 Hz, 2H), 7.09 (s, 2H), 6.93 (t, *J* = 7.4 Hz, 2H), 4.93 (m, 4H), 1.74 (m, 4H), 1.56 (m, 4H), 1.40 (m, 4H). ^{13}C NMR (100 MHz, DMSO-d_6) δ 155.36, 144.13, 139.37, 138.63, 137.79, 135.41, 130.87, 129.23, 128.34, 125.82, 122.18, 121.13, 120.71, 119.23, 115.91, 112.53, 112.03, 50.55, 28.70, 25.94. HRMS m/z: calcd for $C_{46}H_{44}N_4^{2+}$, $[M]^{2+}$ = 326.4336, found 326.1795. HPLC analysis: retention time at 5.141 min eluted with MeOH/H_2O = 50:50 (v/v), purity = 97.6%.

*(E)-1,1'-(octane-1,8-diyl)bis(2-((E)-4-(methylthio)styryl)quinolin-1-ium) iodide (**6**).* Yellow solid with 74% yield. ^{1}H NMR (400 MHz, DMSO-d_6) δ 9.08 (d, *J* = 9.0 Hz, 2H), 8.56 (d, *J* = 9.1 Hz, 2H), 8.52 (d, *J* = 9.1 Hz, 2H), 8.38 (d, *J* = 7.3 Hz, 2H), 8.17 (dd, *J* = 15.3, 7.6 Hz, 4H), 7.96 (t, *J* = 7.6 Hz, 2H), 7.86 (d, *J* = 8.4 Hz, 4H), 7.77 (d, *J* = 15.7 Hz, 2H), 7.31 (d, *J* = 8.4 Hz, 4H), 5.12 – 5.02 (m, 4H), 2.46 (s, 6H), 1.81 (m, 4H), 1.54 (m, 4H), 1.37 (m, 4H). ^{13}C NMR (100 MHz, DMSO-d_6) δ 155.9, 147.59, 144.78, 144.08, 138.70, 135.64, 131.53, 130.94, 130.06, 129.52, 128.64, 125.91, 121.76, 119.49, 117.73, 50.83, 28.98, 28.72, 25.98, 14.49. HRMS m/z: calcd for $C_{44}H_{46}N_2S_2^{2+}$, $[M]^{2+}$ = 333.4892, found 333.1565. HPLC analysis: retention time at 5.142 min eluted with MeOH/H_2O = 50:50 (v/v), purity = 98.2%.

*(E)-1,1'-(octane-1,8-diyl)bis(2-((E)-2-(9-ethyl-9H-carbazol-3-yl)vinyl)quinolin-1-ium) iodide (**7**).* Red solid with 69% yield. ^{1}H NMR (400 MHz, DMSO-d_6) δ 8.65 (s, 2H), 8.60 (d, *J* = 9.0 Hz, 2H), 8.25 (d, *J* = 9.1 Hz, 2H), 8.21 (d, *J* = 9.1 Hz, 2H), 8.14 (d, *J* = 7.4 Hz, 2H), 8.08 (dd, *J* = 11.6, 3.8 Hz, 4H), 8.00 (t, *J* = 7.5 Hz, 2H), 7.95 (d, *J* = 7.7 Hz, 2H), 7.84 (t, *J* = 7.5 Hz, 2H), 7.59 (t, *J* = 11.5 Hz, 4H), 7.42 (d, *J* = 8.2 Hz, 2H), 7.34 (t, *J* = 7.8 Hz, 2H), 7.14 (t, *J* = 7.4 Hz, 2H), 4.85 (m, 4H), 4.26 (q,

J = 6.9 Hz, 4H), 1.64 (m, 8H), 1.55 (m, 4H), 1.18 (t, *J* = 7.1 Hz, 6H). ^{13}C NMR (100 MHz, DMSO-*d*$_6$) δ 155.37, 149.56, 143.46, 141.76, 140.28, 138.18, 135.05, 130.60, 128.85, 128.53, 127.73, 126.95, 126.28, 123.05, 122.26, 120.85, 120.09, 118.81, 114.66, 110.14, 50.04, 37.61, 28.21, 27.92, 25.42, 14.11. HRMS m/z: calcd for $C_{58}H_{56}N_4^{2+}$, $[M]^{2+}$ = 404.2247, found 404.2261. HPLC analysis: retention time at 5.142 min eluted with MeOH/H_2O = 50:50 (v/v), purity = 96.6%.

*(E)-1,1'-(octane-1,8-diyl)bis(2-((E)-4-(pyrrolidin-1-yl)styryl)quinolin-1-ium) iodide (**8**).* Black solid with 70% yield. ^{1}H NMR (400 MHz, DMSO-*d*$_6$) δ 8.71 (d, *J* = 9.2 Hz, 2H), 8.36 (dd, *J* = 9.1, 4.6 Hz, 4H), 8.23 (d, *J* = 7.1 Hz, 2H), 8.11 (d, *J* = 15.2 Hz, 2H), 8.05 (t, *J* = 7.5 Hz, 2H), 7.83 (t, *J* = 7.5 Hz, 2H), 7.68 (d, *J* = 8.7 Hz, 4H), 7.24 (d, *J* = 15.3 Hz, 2H), 6.42 (d, *J* = 8.8 Hz, 4H), 4.85 (m, 4H), 3.09 (m, 8H), 1.88 (m, 8H), 1.85 – 1.75 (m, 4H), 1.64 (m, 4H), 1.50 (m, 4H). ^{13}C NMR (100 MHz, DMSO-*d*$_6$) δ 155.67, 150.58, 149.99, 142.18, 138.60, 134.74, 132.57, 130.51, 128.37, 127.42, 122.40, 120.68, 118.82, 112.46, 110.47, 47.72, 28.30, 25.66, 25.21. HRMS m/z: calcd for $C_{50}H_{56}N_4^{2+}$, $[M]^{2+}$ = 356.5026, found 356.2266. HPLC analysis: retention time at 5.143 min eluted with MeOH/H_2O = 50:50 (v/v), purity = 98.6%.

*(E)-1,1'-(octane-1,8-diyl)bis(2-((E)-4-(piperidin-1-yl)styryl)quinolin-1-ium) iodide (**9**).* Black solid with 71% yield. ^{1}H NMR (400 MHz, DMSO-*d*$_6$) δ 8.84 (d, *J* = 9.1 Hz, 2H), 8.47 (d, *J* = 9.3 Hz, 2H), 8.40 (d, *J* = 9.0 Hz, 2H), 8.28 (d, *J* = 7.5 Hz, 2H), 8.16 (d, *J* = 15.4 Hz, 2H), 8.09 (t, *J* = 7.9 Hz, 2H), 7.87 (t, *J* = 7.5 Hz, 2H), 7.74 (d, *J* = 8.8 Hz, 4H), 7.41 (d, *J* = 15.4 Hz, 2H), 6.90 (d, *J* = 8.8 Hz, 4H), 4.95 (m, 4H), 3.27 (m, 8H), 1.80 (m, 4H), 1.56 (m, 8H), 1.49 (m, 8H), 1.43 (m, 4H). ^{13}C NMR (100 MHz, DMSO-*d*$_6$) δ 155.96, 153.47, 149.27, 142.97, 138.67, 135.00, 132.31, 130.69, 128.71, 127.76, 123.76, 120.98, 119.04, 114.09, 112.31, 49.97, 48.03, 28.61, 25.92, 25.37, 24.35. HRMS m/z: calcd for $C_{52}H_{60}N_4^{2+}$, $[M]^{2+}$ = 370.7409, found 370.2424. HPLC analysis: retention time at 5.144 min eluted with MeOH/H_2O = 50:50 (v/v), purity = 97.8%.

*(E)-1,1'-(octane-1,8-diyl)bis(2-((E)-4-morpholinostyryl)quinolin-1-ium) iodide (**10**).* Black solid with 77% yield. ^{1}H NMR (400 MHz, DMSO-*d*$_6$) δ 8.91 (d, *J* = 9.0 Hz, 2H), 8.51 (d, *J* = 9.2 Hz, 2H), 8.44 (d, *J* = 9.0 Hz, 2H), 8.31 (d, *J* = 7.8 Hz, 2H), 8.19 (d, *J* = 15.4 Hz, 2H), 8.11 (t, *J* = 7.8 Hz, 2H),

7.90 (t, *J* = 7.5 Hz, 2H), 7.79 (d, *J* = 8.6 Hz, 4H), 7.51 (d, *J* = 15.5 Hz, 2H), 6.94 (d, *J* = 8.6 Hz, 4H), 4.99 (m, 4H), 3.68 (t, 8H), 3.20 (t, 8H), 1.81 (m, 4H), 1.57 (m, 4H), 1.41 (m, 4H). ^{13}C NMR (100 MHz, DMSO-d_6) δ 156.03, 153.64, 148.99, 143.46, 138.67, 135.15, 131.90, 130.77, 128.94, 127.96, 125.07, 121.15, 119.18, 114.21, 113.52, 66.21, 50.20, 47.06, 28.69, 25.94. HRMS m/z: calcd for $C_{50}H_{56}N_4O_2^{2+}$, $[M]^{2+}$ = 372.5021, found 372.2215. HPLC analysis: retention time at 5.124 min eluted with MeOH/H_2O = 50:50 (v/v), purity = 95.9%.

*(E)-1-methyl-2-(4-(piperidin-1-yl)styryl)quinolin-1-ium iodide (**11**).* Black solid with 82% yield. ^{1}H NMR (400 MHz, DMSO-d_6) δ 8.85 (d, *J* = 9.1 Hz, 1H), 8.52 (d, *J* = 9.2 Hz, 1H), 8.45 (d, *J* = 9.0 Hz, 1H), 8.25 (dd, *J* = 11.3, 8.4 Hz, 2H), 8.10 (t, *J* = 7.9 Hz, 1H), 7.86 (t, *J* = 8.6 Hz, 3H), 7.60 (d, *J* = 15.5 Hz, 1H), 7.05 (d, *J* = 8.7 Hz, 2H), 4.46 (s, 3H), 3.45 (d, *J* = 4.7 Hz, 4H), 1.62 (m, 6H). ^{13}C NMR (100 MHz, DMSO-d_6) δ 156.8, 153.64, 148.90, 142.63, 139.69, 134.71, 132.44, 130.30, 128.61, 127.40, 123.92, 120.79, 119.38, 114.20, 113.16, 48.18, 25.49, 24.43. HRMS m/z: calcd for $C_{23}H_{25}N_2^+$, $[M]^+$ = 329.4575, found 329.2024. HPLC analysis: retention time at 5.140 min eluted with MeOH/H_2O = 50:50 (v/v), purity = 98.0%.

*(E)-1-butyl-2-(4-(piperidin-1-yl)styryl)quinolin-1-ium iodide (**12**).* Black solid with 75% yield. ^{1}H NMR (400 MHz, DMSO-d_6) δ 8.85 (d, *J* = 9.1 Hz, 1H), 8.55 (d, *J* = 9.2 Hz, 1H), 8.44 (d, *J* = 9.0 Hz, 1H), 8.32 – 8.24 (m, 2H), 8.12 (dd, *J* = 11.7, 4.3 Hz, 1H), 7.86 (dd, *J* = 16.6, 8.3 Hz, 3H), 7.50 (d, *J* = 15.4 Hz, 1H), 7.07 (d, *J* = 9.0 Hz, 2H), 5.10 – 4.96 (m, 2H), 3.47 (d, *J* = 5.4 Hz, 4H), 1.92 – 1.82 (m, 2H), 1.61 (d, *J* = 5.6 Hz, 4H), 1.56 (dd, *J* = 15.1, 7.5 Hz, 4H), 0.99 (t, *J* = 7.3 Hz, 3H). ^{13}C NMR (100 MHz, DMSO-d_6) δ 156.11, 153.69, 149.44, 142.93, 138.76, 135.00, 132.44, 130.65, 128.69, 127.75, 123.84, 120.95, 119.14, 114.27, 112.32, 50.00, 48.22, 30.94, 25.47, 24.46, 19.65, 14.18. HRMS m/z: calcd for $C_{26}H_{31}N_2^+$, $[M]^+$ = 371.5372, found 371.2497. HPLC analysis: retention time at 5.140 min eluted with MeOH/H_2O = 50:50 (v/v), purity = 96.8%.

4.2 Materials and Methods.

All chemicals and reagents used for experiments were AR grade. Hoechst 33342 (Cat. 62249), Mito-Tracker Deep Red (Cat. M22426), Mito-Tracker Green (Cat. M7514), ER-Tracker Blue (Cat.

E12353), Lyso-Tracker Blue (Cat. L7525), MitoSOX Red (Cat. M36005), PI/RNase Staining Solution (Cat. F10797), DNase I (Cat. 18047019) and RNase A (Cat. AM2271) were purchased from Thermo Fisher Scientific. FCCP, Cyclosporin A (CsA), 2MeOE2, KC7F2, DMOG and MitoTEMPOL were purchased from TargetMol. Mitochondrial Permeability Transition Pore Assay Kit (Cat. C2009S) and BeyoFast SYBR Green One-Step qRT-PCR Kit (Cat. D7268M) were purchased from Beyotime Biotechnology. Seahorse XF Glycolysis Stress Test Kit (Cat. 103020-100) and Seahorse XF Cell Mito Stress Test Kit (Cat. 103010-100) were purchased from Agilent. Comet Assay Kit (ab238544) were purchased from Abcam. Annexin V-BUV396 and 7-AAD were purchased from BD Pharmingen. Plasmid were purchased from GenScript. All the oligonucleotides were synthesized and purified by Sangon Biotech and the sequences were listed in Table S1-Table S5. All the antibodies were purchased from Abcam, Cell Signaling Technology and Thermo Fisher Scientific. The cell lines used in this study were purchased from ATCC.

4.2.1 Fluorescence Spectroscopy. Fluorescence spectra were recorded with a LS-45 fluorescence spectrometer (Perkin Elmer). The slit width of the colorimetric dish is 1 mm and optical diameter is 10 mm. The emissions of ligands were acquired by exciting the samples. The emission spectra collection range of ligands was 550-800 nm. All oligonucleotides were pre-annealed by heating at 95 °C for 10 min, followed by slow cooling to room temperature in Tris-HCl buffer (10 mM, pH 7.4) with 100 mM KCl. Small aliquots of a stock solution of oligonucleotides were added into the solution containing ligands at the fixed concentration (5 μM). In the titration studies, the final concentration of oligonucleotides was varied from 0 to 20 μM. After the addition of each sample, the mixture was stirred and allowed to equilibrate for at least 1 min.

4.2.2 UV-Visible Spectroscopy. UV-Vis spectra were obtained using a Lambda 25 Spectrophotometer (Perkin Elmer). The slit width of the colorimetric dish is 1 mm and optical diameter is 10 mm. The absorption spectra collection range of ligands was 300-700 nm. All oligonucleotides were pre-annealed by heating at 95 °C for 10 min, followed by slow cooling to room temperature in Tris-HCl buffer (10 mM, pH 7.4) with 100 mM KCl. Small aliquots of a stock solution

of oligonucleotides were added into the solution containing ligands at the fixed concentration (5 μM). In the titration studies, the final concentration of oligonucleotides was 20 μM. After the addition of each sample, the mixture was stirred and allowed to equilibrate for at least 1 min. The UV spectra of ligands was collected first and then nucleic acids with different concentrations was added in turn (2.5 μM, 5 μM, 10 μM, 15 μM and 20 μM), and the UV spectra were collected, respectively.

4.2.3 Circular Dichroism (CD) and Melting Point Assay. The CD spectra were performed on a JASCO J-1500 Circular Dichroism Spectrometer. In the experiment, a quartz cuvette with a length of 1 mm was used to record the spectrum in a wavelength range of 220 to 700 nm with a 1 nm bandwidth, a 1 nm step and 1 s per point. Each curve was scanned 3 times. After setting the parameters, 400 μL of nucleic acid with a concentration of 5 μM was placed in a colorimetric dish. The CD spectra of nucleic acid were collected first and then **9** with different concentrations was added in turn (5 μM, 10 μM, 15 μM and 20 μM), and the CD spectra were collected, respectively. Melting point assays were set at a fixed wavelength, while gradually increasing the temperature from 25 to 95 °C, 1 nm step size, and 5 s per point. The experiments were performed using 5 μM ligand **9** and 5 μM different nucleic acids in 10 mM Tris-HCl buffer at pH 7.4 containing 20 mM KCl. The collected data were normalized by Origin software.

4.2.4 NMR Spectroscopy. Before taking ^{1}H NMR measurements, *Mito 78* and *Mito 29* with a concentration of 300 μM was dissolved in phosphate buffer (25 mM KH_2PO_4, 10% D_2O, 100 mM KCl, pH = 7.4) and was heated to 95 °C, then annealed to room temperature and incubated for 24 h. During the measurement, ligand **9** with different concentrations was added in turn (150 μM and 300 μM). The experiments were carried out at 25 °C on a 600 MHz spectrometer.

4.2.5 Isothermal Titration Calorimetry (ITC) Assay. ITC experiments were carried out in a MicroCal PEAQ-ITC (Malvern, USA) microcalorimeter. oligonucleotides were pre-annealed in 25 mM KH_2PO_4, 60 mM KCl buffer (pH 7.4, containing 0.2% (v/v) DMSO) by heated to 95 °C in water bath for 5 min. Then, it was cooled to 25 °C and placed at 4 °C overnight. Ligand **9** (10 μM) in buffer

was kept in the sample cell and 40 μL pre-annealed oligonucleotides (100 μM) was filled in the syringe in the same buffer. Ligand **9** was mixed with oligonucleotides by stirring the syringe at 750 rpm at 25 °C. There were 29 injections with a duration of 4 s and an interval of 150 s. Finally, the data were fitted into the built-in binding model to obtain the binding enthalpy.

4.2.6 Surface Plasmon Resonance (SPR) Assay. The immobilization of biotinylated DNA and kinetics assay were performed using Sierra SPR-32 Pro (Bruker). Briefly, biotinylated DNA sequences were dissolved in running buffer (10 mM Tris-HCl, 100 mM KCl, 0.05% Tween 20, pH 7.4). Biotinylated DNA in 800 nM was allowed to immobilize onto biotin capture sensor chip (Bruker Daltonics) with streptavidin chemistry to achieve 800-1000 RU. Different concentrations of ligands were then injected at a flow rate of 30 μL/min for 200 seconds of contact time, followed with 250 seconds of dissociation at 25 °C, using multi-injection cycle kinetics (MICK) mode. The chip was regenerated with injection of 2 M KCl between consecutive cycles. Data was analyzed with Sierra Analyzer R3 software, using kinetics model for fitting data.

4.2.7 Plasmid Construction. cDNAs encoding Pif1, Twinkle and GRSF1 were obtained by gene synthesis from GenScript. To generate eBFP-tagged protein, cDNA was inserted into the pcDNA3.1+ vector.

4.2.8 Cell Culture. The human cancer cell lines including MDA-MB-231 (HTB-26), HeLa (CRM-CCL-2), HepG2 (HB-8065), LoVo (CCL-229), HCT116 (CCL-247), PANC-1 (CRL-1469), human fibroblast HFF-1 (SCRC-1041) and human fibroblast BJ (CRL-2522) were purchased from ATCC. The cell lines were cultured in different complete medium as shown below: MDA-MB-231, HeLa, PANC-1 and HFF1 were cultured in DMEM (Gibco) supplemented with 10% fetal bovine serum (FBS) (Gibco) and 1% P/S (Gibco). LoVo and HCT116 were cultured in RPMI1640 (Gibco) supplemented 10% FBS and 1% P/S. PANC-1 and BJ was cultured in MEM (Gibco) supplemented with 10% FBS and 1% P/S. The cells were incubated in incubator at 37 °C with 5% CO_2. In all experiments needed for cell collection, the cells were trypsinized by 0.25% trypsin-EDTA (Gibco) and suspended in various buffers for further analysis.

4.2.9 MTT Assay. The cancer cells (MDA-MB-231, HeLa, HepG2, LoVo, HCT116 and PANC-1) and normal cells (HFF1 and BJ) were examined in the MTT experiments. The cells were cultured on 96-well plates with a density of 5000 cells per well approximately. The culture condition was set at 37 °C and 5% CO_2. After cultured for 24 h, the cells were treated with ligand s at different concentration (0, 0.625, 1.25, 2.5, 5, 10, 20, 30 and 40 μM) for 48 h, respectively. After incubation, the medium was decanted. Then, 0.5 mg/mL of MTT solution, 100 μL per well, was added to the sample and followed was incubated for 4 h in dark. Then, the MTT solution was decanted and DMSO (100 μL per well) was added to ensure the deck adhering to 96-well plate complete dissolution. These treated 96-well plates were measured for absorbance with an enzyme label and the absorption wavelength was 570 nm. Finally, the cell survival rate and the half maximal inhibitory concentration (IC_{50}) of ligands on the cells were calculated from the obtained absorbance values.

4.2.10 Live-Cell Staining and Imaging Assay. HCT116 cells were cultured in confocal dishes overnight with 5% CO_2 at 37 °C, the RPMI1640 medium containing 10% fetal bovine serum and 1% P/S. The digital images were recorded on Leica TCS SPE Confocal Microscope. In the mitochondria co-location experiment, the cells were treated with 200 nM Mito-Tracker Deep Red for 30 min and 4 μM ligand **9** for 1 h respectively. In the Endoplasmic reticulum co-location experiment, the cells were treated with 1 μM ER-Tracker Blue for 30 min and 4 μM ligand **9** for 1 h respectively. In the Lysosomal co-location experiment, the cells were treated with 1 μM Lyso-Tracker Blue for 30 min and 4 μM ligand **9** for 1 h respectively. In the cyclosporin (CsA) treatment, the cells were treated with 1 μM CsA for 24 h to block the permeability transition pore on the inner membrane of mitochondria. The cells after CsA treatment were washed with RPMI1640 and then the cells were incubated with 4 μM ligand **9** for 1 h and 1 μM Hoechst33342 for 30 min respectively. In the FCCP treatment, the cells were treated with 1 μM FCCP for 30 min to depolarize the cells. After FCCP treatment, the cells were washed with RPMI1640 and then the cells were incubated with 4 μM ligand **9** for 1 h and 1 μM Hoechst33342 for 30 min respectively. In the competition experiments, the cells were incubated with

4 μM ligand **9** for 1 h and 1 μM Hoechst33342 for 30 min respectively, and then 5 μM MitoPDS or 10 μM MitoPDS was added for 3 h. In Cy5-labeled DNA treatments, oligonucleotide transfections were performed using DNA oligonucleotides (4 μg) and Lipofectamine 3000 Transfection Reagent (Invitrogen) for 24 h before staining, and then incubated with 4 μM ligand **9** for 1 h and 1 μM Hoechst33342 for 30 min respectively. In Cy5-labeled DNA and Mito-Tracker Green co-location experiment, Cy5-labeled DNA transfections were performed using DNA oligonucleotides (4 μg) and Lipofectamine 3000 Transfection Reagent (Invitrogen) for 24 h before staining, and then incubated with 200 nM Mito-Tracker Green for 30 min. For the preparation of HCT116 cells overexpressing eBFP-tagged proteins, cells were transfected with the constructed plasmids (4 μg) using Lipofectamine 3000 and then incubated at 37 °C for 24 h, and then incubated with 4 μM ligand **9** for 1 h and 1 μM Hoechst33342 for 30 min respectively. In HIF-1α inhibitors treatment, the cells were treated with 0.1 μM 2-MeOE2, or 10 μM KC7F2 for 24 h before imaging. In HIF-PH inhibitor treatment, the cells were treated with 100 μM for 24 h before imaging. Then the cells were incubated with 4 μM ligand **9** for 1 h and 1 μM Hoechst33342 for 30 min respectively. In mitochondrial membrane potential (MMP) detection, the cells were treated with different concentrations of **9** for 48 h. After treatment, the cells were washed with RPMI1640 and then the cells were treated with 1 μM TMRE for 30 min. In mitochondrial reactive oxygen species (ROS) detection, the cells were treated with different concentrations of **9** with or without 10 μM MitoTEMPOL for 48 h. After treatment, the cells were washed with RPMI1640 and then the cells were treated with 1 μM MitoSOX for 30 min. In mitochondrial permeability transition pore (mPTP) opening detection, the cells were treated with different concentrations of **9** for 48 h. After treatment, the cells were washed with RPMI1640 and then the cells were treated with calcein-AM and $CoCl_2$, respectively.

4.2.11 Fixed Cell Staining Assay. HCT116 cells were cultured in confocal dishes overnight with 5% CO_2 at 37 °C, the RPMI1640 medium containing 10% fetal bovine serum and 1% P/S. The digital images were recorded on Leica TCS SPE Confocal Microscope. In DNase Ⅰ and RNase A digestion

experiments, the cells were incubated with 4 μM ligand **9** for 1 h and 1 μM Hoechst33342 for 30 min respectively before the cells were fixed. After that, the cells were fixed with 4% paraformaldehyde for 20 min, then the cells were infiltrated with 0.3% Triton-X 100/PBS for 1 h. Finally, the cells were incubated with 200 units/mL DNase Ⅰ or RNase A at 37 °C for 3 h. In Lamin B1 immunofluorescence experiment, the cells were treated with different concentrations of **9** for 72 h. After treatment, the medium was removed, cells were fixed with 4% paraformaldehyde in PBS at room temperature for 20 min. The cells were infiltrated with 0.3% Triton-X 100/PBS for 1 h. Then, it was blocked with 1% BSA/PBS for 1 h. After blocking, the cells were incubated with Lamin B1 antibody (Thermofisher Scientific, PA519468, diluted 1:1000) at 4 °C overnight. After overnight incubation, the cells were washed with pre-cooled PBS for 3 times and were incubated with incubated with Goat anti-Rabbit IgG Alexa Fluor 647 (ThermoFisher Scientific, A-21245, diluted 1:1000) for another 1 h. After secondary antibody incubation, the cells were washed with pre-cooled TBST for 3 times and then treated with 1 μM Hoechst33342 for 30 min. In Ki67 immunofluorescence experiment, the cells were treated with different concentrations of **9** for 72 h. After treatment, the medium was removed, cells were fixed with 4% paraformaldehyde in PBS at room temperature for 20 min. The cells were infiltrated with 0.3% Triton-X 100/PBS for 1 h. Then, it was blocked with 1% BSA/PBS for 1 h. After blocking, the cells were incubated with Ki67 antibody (Beyotime Biotechnology, AF1738, diluted 1:500) at 4 °C overnight. After overnight incubation, the cells were washed with pre-cooled PBS for 3 times and were incubated with incubated with Goat anti-Rabbit IgG Alexa Fluor 647 (ThermoFisher Scientific, A-21245, diluted 1:1000) for another 1 h. After secondary antibody incubation, the cells were washed with pre-cooled TBST for 3 times and then treated with 1 μM Hoechst33342 for 30 min. In BG4 immunofluorescence experiment, Cy5-labeled DNA transfections were performed using DNA oligonucleotides (4 μg) and Lipofectamine 3000 Transfection Reagent (Invitrogen) for 24 h. After transfection, the medium was removed, cells were fixed with 4% paraformaldehyde in PBS at room temperature for 20 min. The cells were infiltrated with 0.3% Triton-X 100/PBS for 1 h. Then, it was blocked with 1% BSA/PBS for 1 h. After blocking, the cells were

incubated with BG4 antibody (EMD Millipore Corporation, MABE917, diluted 1:1000) at 4 °C overnight. After overnight incubation, the cells were washed with pre-cooled PBS for 3 times and were incubated with rabbit anti-FLAG (CST, 2368, diluted 1:1000) at room temperature for 1 h. After secondary antibody incubation, the cells were washed with pre-cooled PBS for 3 times. The cells were further incubated with goat anti-rabbit IgG Alexa Fluor 488 (ThermoFisher Scientific, A-11008, diluted 1:500) for another 1 h. Finally, the cells were washed with pre-cooled TBST for 3 times.

4.2.12 Cell Cycle Analysis. In the experiment, PI was used to detect the cell cycle of HCT116 cells. Firstly, cells were collected at a density of 5 x 10^5 cells/mL after incubated with different concentration of **9** for 72 h, then cells were fixed with 70% ethanol in PBS at 4 °C for 2 h. After that, cells were stained with PI. Finally, the cells were analyzed by flow cytometry (BD Accuri C6 Flow Cytometer).

4.2.13 Cell Apoptosis Analysis. HCT116 cells were seeded at density 1 x 10^5 cells/flask in a 25-cm^2 culture flask (TPP). After overnight incubation, the cells were treated with **9** at different concentrations for 72 h. After treatment, the cells were collected by trypsinization with 0.25% trypsin with EDTA and suspended in PBS. The cells were then treated with Annexin V-BUV39 and 7-AAD (BD Pharmingen) according to the manufacturer's instructions. The treated cells were subjected to flow cytometry (BD FACSymphony A3 Cell Analyzer) for apoptotic analysis.

4.2.14 Comet Assay for DNA Damage Detection. The DNA damage in HCT116 cells was detected by Comet assay kit (Abcam, ab238544). After overnight incubation, the cells were treated with different concentrations of **9** with or without 10 μM MitoTEMPOL for 72 h. After treatment, the cells were collected by trypsinization with 0.25% trypsin with EDTA and suspended in ice-cold PBS at 1x10^5 cells/mL. The sample was prepared according to the manufacturer's instruction. Briefly, cells were mixed with comet agarose at 37 °C and pipetted the agarose/cell mixture onto the top of the base layer of comet agarose. The slide was transferred to 4 °C in the dark for 15 minutes for gelation. The slide was then transferred to a container with pre-chilled lysis buffer for 30 minutes at 4 °C in the dark. After lysis buffer treatment, the slide was treated with alkaline solution for 30 minutes at

4 °C in the dark. The treated slide was then transferred to a horizontal electrophoresis chamber for electrophoresis under alkaline electrophoresis solution (300 mM NaOH and 1 mM EDTA, pH > 13), with 30 V for 30 minutes. The slide was washed twice with cold water and immersed in cold 70 % ethanol for 5 minutes. The slide was then allowed to air dry and was treated with 1 μM DAPI for 10 minutes. The slide was subjected to Ti2-E Live-cell fluorescence imaging system (Nikon) with 405 nm excitation LED for imaging. The tail moment length is measured from the center of the head to the center of the tail.

4.2.15 *β*-Galactosidase (SA-*β*-gal) Staining of Cell Senescence. HCT116 cells were cultured in a 6-well plate and were treated with different concentrations of **9** for 72 h. Then, the medium was removed and the cells were washed with PBS 3 times. The *β*-galactosidase staining fixative was added and fixed at room temperature for 15 min. Then, the cell fixative was removed and washed three times with PBS for 3 min each time. After that, the working solution of *β*-galactosidase staining was added and incubated at 37 °C overnight. Finally, the data were observed and collected under an inverted fluorescence microscope (Olympus IX71).

4.2.16 Detection of *β*-Galactosidase Activity. In this assay, Senescence *β*-Galactosidase Activity Assay Kit (Fluorescence, Plate-Based, CST) was used to detect the *β*-Galactosidase activity. Briefly, HCT116 cells were cultured in a 6-well plate and were treated with different concentrations of **9** for 72 h. Then, the medium was removed and the cells were washed with cold PBS for 1 time. After that, the cells were processed according to the manufacturer's instruction. Finally, the samples were measured at an excitation wavelength of 360 nm and an emission wavelength of 465 nm.

4.2.17 RNA Isolation and qRT-PCR. HCT116 cells or HFF1 cells were seeded at density 1 x 10^5 cells/flask in a 25-cm^2 culture flask (TPP). After overnight incubation, the cells were treated with different concentrations of **9** for 48 h. After treatment, the cells were trypsinized and subjected to RNA extraction with RNase Mini kit (Qiagen). The RNA samples were prepared according to the manufacturer's instructions (BeyoFast SYBR Green One-Step qRT-PCR Kit, Beyotime Biotechnology). Each reaction mixture (20 μL) contained 2x One Step SYBR Green Mix 10 μL, One

Step SYBR Green Enzyme Mix 1 μL, 50x ROX Reference Dye 1 0.4 μL, Gene Specific Primer Forward (0.3 μM) 1 μL, Gene Specific Primer Reverse (0.3 μM) 1 μL, 50 ng of total RNA and RNase-free ddH_2O to 20 μL. The reaction mixtures were incubated in a thermocycler under the following cycling conditions: reverse transcription at 50 °C for 30 min, denature at 95 °C for 2 min, followed by 40 cycles at 95 °C for 15 s and 60 °C for 30 s.

4.2.18 DNA Isolation and q-PCR. HCT116 cells or HFF1 cells were seeded at density 1 x 10^5 cells/flask in a 25-cm^2 culture flask (TPP). After overnight incubation, the cells were treated with different concentrations of **9** for 48 h. After treatment, the cells were trypsinized and subjected to PureLink Genomic DNA Mini Kit (ThermoFisher Scientific). The DNA samples were prepared according to the manufacturer's instructions (PowerUp SYBR Green Master Mix for qPCR, ThermoFisher Scientific). Each reaction mixture (20 μL) contained 2x SYBR Green Master Mix 10 μL, Gene Specific Primer Forward (0.3 μM) 1 μL, Gene Specific Primer Reverse (0.3 μM) 1 μL, 50 ng of total DNA and RNase-free ddH_2O to 20 μL. The reaction mixtures were incubated in a thermocycler under the following cycling conditions: UDG activation at 50 °C for 2 min, activation (Dual-Lock DNA polymerase) at 95 °C for 2 min, followed by 40 cycles at 95 °C for 15 s and 60 °C for 1 min.

4.2.19 Western Blotting. HCT116 cells were seeded at density 80 x 10^4 cells/flask in a 25-cm^2 culture flask (TPP). After overnight incubation, the cells were treated different concentrations of **9** for 48 or 72 h. The cells were collected and incubated on ice for 20 min in the RIPA buffer (containing protease inhibitors and phosphatase inhibitors), then at 4 °C, 12000 × g for 10 minutes. The total protein concentration was quantified by BCA kit. The same amount of protein (30 μg) was loaded onto the SDS-PAGE gel (12%) and the separated protein was transferred to the PVDF membrane. After blocking with 5% skim milk, the membranes were incubated with primary antibodies against MT-ND1 (Abcam, ab219821, diluted 1:1000), MT-ND2 (Abcam, ab181848, diluted 1:1000), MT-ND3 (CST, 82933S, diluted 1:1000), MT-ND4 (ThermoFisher Scientific, PA5-114379, diluted 1:1000), MT-ND4L (ThermoFisher Scientific, PA5103953, diluted 1:1000), MT-ND5 (Abcam, ab230509,

diluted 1:1000), MT-ND6 (ThermoFisher Scientific, PA5-109993, diluted 1:1000), MT-COX1 (CST, 55159S, diluted 1:1000), MT-COX2 (CST, 50003S, diluted 1:1000), MT-COX3 (ThermoFisher Scientific, 459300, diluted 1:1000), Cytochrome b (CST, 54618S, diluted 1:1000), MT-ATP6 (CST, 70262S, diluted 1:1000), MT-ATP8 (CST, 96857S, diluted 1:1000), Total OXPHOS Human WB antibody Cocktail (Abcam, ab110411, diluted 1:1000), Lamin B1 (CST, 13435S, diluted 1:1000), p53 (CST, 2527S, diluted 1:1000), p21 (CST, 2947S, diluted 1:1000), p16 (CST, 92803S, diluted 1:1000), γ-H2A.x (CST, 9718S, diluted 1:1000), Caspase3 (Abcam, ab32351, diluted 1:1000), Cleaved-Caspase3 (Abcam, ab32042, diluted 1:1000), and β-actin (Abcam, ab8226, diluted 1:5000) respectively overnight at 4 °C. The membranes were washed three times with TBST buffer for 0.5 h, then incubated with Anti-mouse IgG, HRP-linked Antibody (CST, 7076S, diluted 1:5000) or Anti-rabbit IgG, HRP-linked Antibody (CST, 7074S, diluted 1:5000) at room temperature for 2 h. After incubation, membranes were extensively washed and subjected to chemiluminescence detection with Immobilon Western Chemiluminescent HRP substrate (Merck Millipore).

4.2.20 Seahorse Experiment. For Mito Stress Test, at day 1, HCT116 cells in RPMI1640 were seeded at density 5 x 10^4 cells/well in a 24-well Agilent Seahorse XF cell culture microplate (Agilent Technologies) overnight. The wells of A1, B4, C3 and D6 were filled with medium only as the reference wells. The sensor cartridge on the calibration plate (Agilent Technologies) was calibrated with 1 mL of Agilent Seahorse XF Calibrant (Agilent Technologies). The calibration plate was placed into a non-CO_2 37 °C incubator overnight. At day 2, RPMI1640 was removed from the microplate prepared and then the cells were treated with different concentrations of **9** for 3 h. After that, 500 μL of assay medium (RPMI1640 assay medium provided by Agilent Technology supplemented with 1 mM pyruvate, 2 mM glutamine and 10 mM D-glucose, pH 7.4 at 37 °C) were added to each well. The microplates with cells were placed into a non-CO_2 incubator at 37 °C for 1 h. Besides, the sensor cartridges on the calibration plate prepared at day 1 were loaded with different ligands in assay medium (port A: 56 μL 10 μM oligomycin; port B: 62 μL of 10 μM FCCP; port C: 69 μL of 10 μM of 5 μM rotenone and 5 μM antimycin A). The loaded sensor cartridge on the calibration plate was

placed in a XF24 analyzer (Agilent Technologies) for 30 min. After incubation, the calibration plate was replaced with the microplate with cells. The Seahorse software Wave was used to perform the Mito Stress Test.

For Glycolysis Stress Test, HCT116 cells in RPMI1640 were seeded at density 5 x 10^4 cells/well in a 24-well Agilent Seahorse XF cell culture microplate (Agilent Technologies) overnight. The wells of A1, B4, C3 and D6 were filled with medium only as the reference wells. The sensor cartridge on the calibration plate (Agilent Technologies) was calibrated with 1 mL of Agilent Seahorse XF Calibrant (Agilent Technologies). The calibration plate was placed into a non-CO_2 37 °C incubator overnight. At day 2, RPMI1640 was removed from the microplate prepared and then the cells were treated with different concentrations of **9** for 3 h. After that, 500 μL of assay medium (RPMI1640 assay medium provided by Agilent Technology supplemented with 2 mM glutamine, pH 7.4 at 37 °C) were added to each well. The microplates with cells were placed into a non-CO_2 incubator at 37 °C for 1 h. Besides, the sensor cartridges on the calibration plate prepared at day 1 were loaded with different ligands in assay medium (port A: 56 μL 100 mM glucose; port B: 62 μL of 10 μM oligomycin; port C: 69 μL 500 mM 2-DG). The loaded sensor cartridge on the calibration plate was placed in a XF24 analyzer (Agilent Technologies) for 30 min. After incubation, the calibration plate was replaced with microplates with cells. The Seahorse software Wave was used to perform Glycolysis Stress Tests.

4.2.21 RNA-sequencing (RNA-seq). HCT116 cells were seeded at density 1 x 10^5 cells/flask in a 25-cm^2 culture flask (TPP). After overnight incubation, the cells were treated with 4 μM ligand **9** for 48 h. After treatment, the cells were trypsinized and subjected to RNA extraction with RNase Mini kit (Qiagen). The RNA samples were prepared according to the manufacturer's instructions. After that, the RNA samples were sent to Novogene company for RNA sequencing and data analysis. The raw transcriptome data have been deposited in NCBI Sequence Read Archive (SRA) database (BioProject: PRJNA1067376). Briefly, the quantity and quality of RNA samples were assessed by Qubit 4.0 fluorometer (ThermoFisher Scientific) and Agilent 2100 Bioanalyzer (Agilent) respectively.

cDNA libraries were prepared from RNA samples with Illumina TruSeq Stranded Total RNA Prep kit (ligation with Ribo-Zero Plus) and indexing kit (Illumina). The quantity and quality of prepared cDNA libraries were assessed by Qubit 4.0 fluorometer and Agilent 2100 Bioanalyzer respectively. The cDNA libraries of experimental and control groups were pooled, and the sequencing was done by Illumina NextSeq 2000 system with 150bp paired-end dual-indexed method. The sequencing quality of the experimental and control samples was determined by FastQC. The low-quality reads and adapter sequences were trimmed with Fastp. The trimmed reads were further aligned to human reference genome (GRCh38/hg38) with STAR package (R programming). The STAR output (reads per gene) was subjected to DESeq2 (R programming) to perform differential expression analysis. Genes with fold-change>1 or <−1 and p-value <0.05 were defined as differentially expressed genes. By this criterion, a heat map of expression patterns was generated in R (pheatmap). The volcano plot was drawn with R (ggplot2). Kyoto Encyclopedia of Genes and Genomes (KEGG) analysis was performed with clusterprofiler (R programming). Gene Set Enrichment Analysis (GSEA) was carried out using the GSEA software 4.1.0 (Broad Institute) with hallmark gene sets (H collection) and canonical pathways gene sets (CP in C2 collection) in Molecular Signatures Database (MSigDB 7.2).

4.2.22 Colony Formation Assay. In 6-well plates, 500 HCT116 cells were seeded in RPMI1640 and incubated with different concentrations of **9** for 7 days. The samples were then treated with crystal violet (Beyotime Biotechnology) for 30 min. Finally, the plates were dried and photographed, and the colony numbers were counted ImageJ.

4.2.23 Trans-well Assay. Trans-well migration assay was performed using Trans-well chambers. A total of 10^5 HCT116 cells were seeded in the upper chamber of a 24-well plate in 200 μL of serum-free RPMI1640 medium. The lower chamber was filled with 600 μL of RPMI1640 medium containing 20% FBS. The chamber was incubated with different concentrations of **9** at 37 °C for 72 h. At the end of incubation, cells in the upper surface of the membrane were removed with a cotton swab. Migrated cells on the lower surface of the membrane were treated with crystal violet. Cells were observed under microscope.

4.2.24 *In Vivo* Antitumor Activity in the Human Colorectal Cancer (HCT116) Xenograft Model. All animal experiments performed in the present study were in compliance with the Animal Management Rules of the Ministry of Health of the People's Republic of China, and also were in compliance with the institutional ethics committee regulations and guidelines on animal welfare. The approved ASESC (Animal Subjects Ethics Sub-Committee) Case Number is 21-22/45-ABCT-R-GRF. The experiments were performed with 2% isoflurane to minimize suffering. In the study, male Balb/c nude mice (18–20 g) were placed in small animal isolators under aseptic conditions to obtain food and water freely. All animal care and procedures were approved by the university ethics committee for use in laboratory animals. To establish a xenograft model, it was injected subcutaneously with HCT116 cell suspension (5×10^6 cells). When the subcutaneous tumor diameter was 100 mm^3, the nude mice were divided into two groups (6 mice per group): tail vein injection of PBS (control group) and **9** (treatment group). The ligand dose in treatment group was 5 mg/kg, injected every two days. Mice were executed on the 16th day after intravenous injection of the ligand. Samples of blood were collected, centrifuged and separated into cell and serum fractions for routine blood data. Major organs and tumor tissues were taken from each group for hematoxylin and eosin (H&E) staining, TUNEL staining, and Ki67 staining.

4.2.25 Statistical Test. Statistical details including the number of biological replicates (n) and *p* values are detailed in figure legends. Data in bar graphs are shown as an absolute number with means ± SD noted. Wilcoxon-Mann-Whitney test was used to calculate significant differences where indicated. $p < 0.05$ was considered statistically significant; ns, not significant. The criterion for statistical significance was taken as ns: $p > 0.05$, $*p < 0.05$, $**p < 0.01$, $***p < 0.001$.

ASSOCIATED CONTENE

Supporting Information

The Supporting Information is available free of charge at

Supplementary figures and tables for the results discussed in the paper and the characterizations of new compounds synthesized in the present study (PDF).

Molecular formula string for the compounds **1-12** (CSV).

AUTHOR INFORMATION

Corresponding Author

Wing-Leung Wong - State Key Laboratory of Chemical Biology and Drug Discovery, Department of Applied Biology and Chemical Technology, The Hong Kong Polytechnic University, Hung Hom, Kowloon, Hong Kong SAR, 999077, China. The Hong Kong Polytechnic University Shenzhen Research Institute, Shenzhen 518057, P. R. China. ORCID https://orcid.org/0000-0001-7191-7578 Email: wing.leung.wong@polyuy.edu.hk

Authors

Bo-Xin Zheng - State Key Laboratory of Chemical Biology and Drug Discovery, Department of Applied Biology and Chemical Technology, The Hong Kong Polytechnic University, Hung Hom, Kowloon, Hong Kong SAR, 999077, China. ORCID: https://orcid.org/0009-0001-0191-9719

Wei Long - State Key Laboratory of Chemical Biology and Drug Discovery, Department of Applied Biology and Chemical Technology, The Hong Kong Polytechnic University, Hung Hom, Kowloon, Hong Kong SAR, 999077, China. ORCID: https://orcid.org/0000-0003-4739-2008

Wende Zheng - The Hong Kong Polytechnic University Shenzhen Research Institute, Shenzhen 518057, P. R. China. ORCID: https://orcid.org/0009-0003-3747-6352

Yaoxun Zeng - The Hong Kong Polytechnic University Shenzhen Research Institute, Shenzhen 518057, P. R. China. ORCID: https://orcid.org/0000-0002-1775-7339

Xiao-Chun Guo - School of Biomedical and Pharmaceutical Sciences, Guangdong University of Technology, Guangzhou 510006, P. R. China. ORCID: https://orcid.org/0000-0002-7150-6450

Ka-Hin Chan - State Key Laboratory of Chemical Biology and Drug Discovery, Department of Applied Biology and Chemical Technology, The Hong Kong Polytechnic University, Hung Hom, Kowloon, Hong Kong SAR, 999077, China. ORCID: https://orcid.org/0000-0003-0860-0361

Meng-Ting She - The Hong Kong Polytechnic University Shenzhen Research Institute, Shenzhen 518057, P. R. China. ORCID: https://orcid.org/0009-0007-7237-4609

Alan Siu-Lun Leung - State Key Laboratory of Chemical Biology and Drug Discovery, Department of Applied Biology and Chemical Technology, The Hong Kong Polytechnic University, Hung Hom, Kowloon, Hong Kong SAR, 999077, China.

Yu-Jing Lu - School of Biomedical and Pharmaceutical Sciences, Guangdong University of Technology, Guangzhou 510006, P. R. China. ORCID: https://orcid.org/0000-0003-2494-843X

Author Contributions

All authors are contributed equally in the present study.

Notes

The authors declare no competing financial interest.

ACKNOWLEDGMENTS

The work described in this paper was fully supported by a grant from the Research Grants Council of the Hong Kong Special Administrative Region, China (RGC Project No. 15300522). W.L. acknowledges the award of a postdoctoral fellowship administered by the Research Committee of The Hong Kong Polytechnic University. We acknowledged Dr. Chan Chun-ming, Fortune, Scientific Officer of the Deparatment of Applied Biology and Chemical Biology, The Hong Kong Polytechnic University, for his kind assistance provided in the NMR study. We also acknowledged Dr. Xiu-Cai Chen, Associate Professor of Guangdong University of Technology, for providing us the compound MitoPDS. The University Research Facilities on Life Sciences and Chemical and Environmental Analysis of The Hong Kong Polytechnic University are acknowledged.

ABBREVIATIONS

2-DG, 2-Deoxy-D-glucose; 2MeOE2, 2-methoxy-13-methyl-7,8,9,11,12,13,14,15,16,17-decahydro-6H-cyclopenta[a]phenanthrene-3,17-diol; 7-AAD, 7-aminoactinomycin D; BMVC-12-P, 3,6-Bis-(1-methyl-2 vinylpyridium iodide)-9-(1-(1 methyl-Piperidinium iodide)dodecyl) carbazole; DMEM, Dulbecco's Modified Eagle Medium; DMOG, dimethyloxalylglycine; DMSO, dimethyl sulfoxide; DODC, 5-(3-Ethylbenzoxazol-2-ylidene)-1-(3-ethylbenzoxazolium-2-yl)-1,3-pentadiene iodide; FBS, fetal bovine serum; FDR, false discovery rate; Hoechst 33342, 2'-(4-ethoxyphenyl)-6-(4-methylpiperazin-1-yl)-1H,3'H-2,5'-bibenzo[d]imidazole; KC7F2, N,N'-(disulfanediylbis(ethane-2,1-diyl))bis(2,5-dichlorobenzenesulfonamide); MEM, Minimum Essential Media; MitoPDS, (4-(4-(((2-((2,6-bis((4-(2-aminoethoxy)quinolin-2-yl)carbamoyl)pyridin-4-yl)oxy)ethyl)amino)methyl)-1H-1,2,3-triazol-1-yl)butyl)triphenylphosphonium iodide; MitoSOX, (6-(3,8-diamino-6-phenylphenanthridin-5(6H)-yl)hexyl)triphenylphosphonium iodide; MitoTEMPOL, 4-hydroxy-2,2,6,6-tetramethylpiperidine 1-oxyl; MTT, 3-(4,5-dimethylthiazol-2-yl)-2,5-diphenyltetrazolium bromide; PAGE, polyacrylamide gel electrophoresis; PBS, phosphate-buffered saline; PI, propidium iodide; RPMI1640, Roswell Park Memorial Institute 1640 Medium; $TMPyP_4$, 5,10,15,20-Tetrakis-(N-methyl-4-pyridyl)porphine; TMRE, tetramethylrhodamine ethyl ester perchlorate;

REFERENCES

1. Burge, S.; Parkinson, G. N.; Hazel, P.; Todd, A. K.; Neidle, S., Quadruplex DNA: sequence, topology and structure. *Nucleic Acids Res* **2006,** *34* (19), 5402-5415.
2. Gellert, M.; Lipsett, M. N.; Davies, D. R., Helix formation by guanylic acid. *Proc Natl Acad Sci U S A* **1962,** *48* (12), 2013-2018.
3. Sen, D.; Gilbert, W., Formation of parallel four-stranded complexes by guanine-rich motifs in DNA and its implications for meiosis. *Nature* **1988,** *334* (6180), 364-366.
4. Guo, J. U.; Bartel, D. P., RNA G-quadruplexes are globally unfolded in eukaryotic cells and depleted in bacteria. *Science* **2016,** *353* (6306), aaf5371.
5. Bochman, M. L.; Paeschke, K.; Zakian, V. A., DNA secondary structures: stability and function of G-quadruplex structures. *Nat Rev Genet* **2012,** *13* (11), 770-780.
6. Yan, M. P.; Wee, C. E.; Yen, K. P.; Stevens, A.; Wai, L. K., G-quadruplex ligands as therapeutic agents against cancer, neurological disorders and viral infections. *Future Medicinal Chemistry* **2023,** *15* (21), 1987-2009.
7. Balasubramanian, S.; Hurley, L. H.; Neidle, S., Targeting G-quadruplexes in gene promoters: a novel anticancer strategy? *Nat Rev Drug Discov* **2011,** *10* (4), 261-275.

8. Nakanishi, C.; Seimiya, H., G-quadruplex in cancer biology and drug discovery. *Biochemical and Biophysical Research Communications* **2020,** *531* (1), 45-50.
9. Chen, L.; Dickerhoff, J.; Sakai, S.; Yang, D., DNA G-Quadruplex in Human Telomeres and Oncogene Promoters: Structures, Functions, and Small Molecule Targeting. *Accounts of Chemical Research* **2022,** *55* (18), 2628-2646.
10. Carvalho, J.; Mergny, J. L.; Salgado, G. F.; Queiroz, J. A.; Cruz, C., G-quadruplex, Friend or Foe: The Role of the G-quartet in Anticancer Strategies. *Trends Mol Med* **2020,** *26* (9), 848-861.
11. Debbarma, S.; Acharya, P. C., Targeting G-Quadruplex DNA for Cancer Chemotherapy. *Curr Drug Discov Technol* **2022,** *19* (3), e140222201110.
12. Long, W.; Zheng, B.-X.; Li, Y.; Huang, X.-H.; Lin, D.-M.; Chen, C.-C.; Hou, J.-Q.; Ou, T.-M.; Wong, W.-L.; Zhang, K.; Lu, Y.-J., Rational design of small-molecules to recognize G-quadruplexes of c-MYC promoter and telomere and the evaluation of their in vivo antitumor activity against breast cancer. *Nucleic Acids Research* **2022,** *50* (4), 1829-1848.
13. Liu, Y.; Sun, Y.; Guo, Y.; Shi, X.; Chen, X.; Feng, W.; Wu, L. L.; Zhang, J.; Yu, S.; Wang, Y.; Shi, Y., An Overview: The Diversified Role of Mitochondria in Cancer Metabolism. *Int J Biol Sci* **2023,** *19* (3), 897-915.
14. Vyas, S.; Zaganjor, E.; Haigis, M. C., Mitochondria and Cancer. *Cell* **2016,** *166* (3), 555-566.
15. Wallace, D. C., Mitochondria and cancer. *Nature Reviews Cancer* **2012,** *12* (10), 685-698.
16. Gorman, G. S.; Chinnery, P. F.; DiMauro, S.; Hirano, M.; Koga, Y.; McFarland, R.; Suomalainen, A.; Thorburn, D. R.; Zeviani, M.; Turnbull, D. M., Mitochondrial diseases. *Nature Reviews Disease Primers* **2016,** *2* (1), 16080.
17. Falabella, M.; Fernandez, R. J.; Johnson, F. B.; Kaufman, B. A., Potential Roles for G-Quadruplexes in Mitochondria. *Curr Med Chem* **2019,** *26* (16), 2918-2932.
18. Sahayasheela, V. J.; Yu, Z.; Hidaka, T.; Pandian, G. N.; Sugiyama, H., Mitochondria and G-quadruplex evolution: an intertwined relationship. *Trends in Genetics* **2023,** *39* (1), 15-30.
19. Bedrat, A.; Lacroix, L.; Mergny, J.-L., Re-evaluation of G-quadruplex propensity with G4Hunter. *Nucleic Acids Research* **2016,** *44* (4), 1746-1759.
20. Bharti, S. K.; Sommers, J. A.; Zhou, J.; Kaplan, D. L.; Spelbrink, J. N.; Mergny, J.-L.; Brosh, R. M., Jr., DNA Sequences Proximal to Human Mitochondrial DNA Deletion Breakpoints Prevalent in Human Disease Form G-quadruplexes, a Class of DNA Structures Inefficiently Unwound by the Mitochondrial Replicative Twinkle Helicase *. *Journal of Biological Chemistry* **2014,** *289* (43), 29975-29993.
21. Doimo, M.; Chaudhari, N.; Abrahamsson, S.; L'Hôte, V.; Nguyen, Tran V. H.; Berner, A.; Ndi, M.; Abrahamsson, A.; Das, Rabindra N.; Aasumets, K.; Goffart, S.; Pohjoismäki, J. L. O.; López, M. D.; Chorell, E.; Wanrooij, S., Enhanced mitochondrial G-quadruplex formation impedes replication fork progression leading to mtDNA loss in human cells. *Nucleic Acids Research* **2023,** *51* (14), 7392-7408.
22. Dong, D. W.; Pereira, F.; Barrett, S. P.; Kolesar, J. E.; Cao, K.; Damas, J.; Yatsunyk, L. A.; Johnson, F. B.; Kaufman, B. A., Association of G-quadruplex forming sequences with human mtDNA deletion breakpoints. *BMC Genomics* **2014,** *15* (1), 677.
23. Chen, X.-C.; Tang, G.-X.; Luo, W.-H.; Shao, W.; Dai, J.; Zeng, S.-T.; Huang, Z.-S.; Chen, S.-B.; Tan, J.-H., Monitoring and Modulating mtDNA G-Quadruplex Dynamics Reveal Its Close Relationship to Cell Glycolysis. *Journal of the American Chemical Society* **2021,** *143* (49), 20779-20791.
24. She, M.-T.; Yang, J.-W.; Zheng, B.-X.; Long, W.; Huang, X.-H.; Luo, J.-R.; Chen, Z.-X.; Liu, A.-L.; Cai, D.-P.; Wong, W.-L.; Lu, Y.-J., Design mitochondria-specific fluorescent turn-on probes targeting G-quadruplexes for live cell imaging and mitophagy monitoring study. *Chemical Engineering Journal* **2022,** *446*, 136947.
25. Agaronyan, K.; Morozov, Y. I.; Anikin, M.; Temiakov, D., Replication-transcription switch in human mitochondria. *Science* **2015,** *347* (6221), 548-551.
26. Annesley, S. J.; Fisher, P. R., Mitochondria in Health and Disease. *Cells* **2019,** *8* (7), 680.
27. Popov, L.-D., Mitochondrial biogenesis: An update. *Journal of Cellular and Molecular Medicine* **2020,** *24* (9), 4892-4899.
28. Grasso, D.; Zampieri, L. X.; Capelôa, T.; Van de Velde, J. A.; Sonveaux, P., Mitochondria in cancer. *Cell Stress* **2020,** *4* (6), 114-146.
29. Moro, L., Mitochondrial Dysfunction in Aging and Cancer. *Journal of Clinical Medicine* **2019,** *8* (11), 1983.

30. Wang, S.-F.; Tseng, L.-M.; Lee, H.-C., Role of mitochondrial alterations in human cancer progression and cancer immunity. *Journal of Biomedical Science* **2023,** *30* (1), 61.
31. Cui, Q.; Wen, S.; Huang, P., Targeting cancer cell mitochondria as a therapeutic approach: recent updates. *Future Med Chem* **2017,** *9* (9), 929-949.
32. Dong, L.; Neuzil, J., Targeting mitochondria as an anticancer strategy. *Cancer Commun (Lond)* **2019,** *39* (1), 63.
33. Fulda, S.; Galluzzi, L.; Kroemer, G., Targeting mitochondria for cancer therapy. *Nat Rev Drug Discov* **2010,** *9* (6), 447-464.
34. Zielonka, J.; Joseph, J.; Sikora, A.; Hardy, M.; Ouari, O.; Vasquez-Vivar, J.; Cheng, G.; Lopez, M.; Kalyanaraman, B., Mitochondria-Targeted Triphenylphosphonium-Based Compounds: Syntheses, Mechanisms of Action, and Therapeutic and Diagnostic Applications. *Chemical Reviews* **2017,** *117* (15), 10043-10120.
35. Cheng, X.; Feng, D.; Lv, J.; Cui, X.; Wang, Y.; Wang, Q.; Zhang, L., Application Prospects of Triphenylphosphine-Based Mitochondria-Targeted Cancer Therapy. *Cancers* **2023,** *15* (3), 666.
36. Huang, W.-C.; Tseng, T.-Y.; Chen, Y.-T.; Chang, C.-C.; Wang, Z.-F.; Wang, C.-L.; Hsu, T.-N.; Li, P.-T.; Chen, C.-T.; Lin, J.-J.; Lou, P.-J.; Chang, T.-C., Direct evidence of mitochondrial G-quadruplex DNA by using fluorescent anti-cancer agents. *Nucleic Acids Research* **2015,** *43* (21), 10102-10113.
37. Zhuang, X.-Y.; Yao, Y.-G., Mitochondrial dysfunction and nuclear-mitochondrial shuttling of TERT are involved in cell proliferation arrest induced by G-quadruplex ligands. *FEBS Letters* **2013,** *587* (11), 1656-1662.
38. Zheng, B.-X.; Yu, J.; Long, W.; Chan, K. H.; Leung, A. S.-L.; Wong, W.-L., Structurally diverse G-quadruplexes as the noncanonical nucleic acid drug target for live cell imaging and antibacterial study. *Chemical Communications* **2023,** *59* (11), 1415-1433.
39. Kumar, P.; Pandith, A.; Tseng, C.-L.; Burnouf, T., Recent Developments in Mitochondrial G-Quadruplex Recognising Fluorescent Probes: A Review. *Journal of Photochemistry and Photobiology C: Photochemistry Reviews* **2023,** *56*, 100619.
40. Kulkarni, C. A.; Fink, B. D.; Gibbs, B. E.; Chheda, P. R.; Wu, M.; Sivitz, W. I.; Kerns, R. J., A Novel Triphenylphosphonium Carrier to Target Mitochondria without Uncoupling Oxidative Phosphorylation. *Journal of Medicinal Chemistry* **2021,** *64* (1), 662-676.
41. Zorova, L. D.; Popkov, V. A.; Plotnikov, E. Y.; Silachev, D. N.; Pevzner, I. B.; Jankauskas, S. S.; Babenko, V. A.; Zorov, S. D.; Balakireva, A. V.; Juhaszova, M.; Sollott, S. J.; Zorov, D. B., Mitochondrial membrane potential. *Anal Biochem* **2018,** *552*, 50-59.
42. Wang, J.; Li, J.; Xiao, Y.; Fu, B.; Qin, Z., TPP-based mitocans: a potent strategy for anticancer drug design. *RSC Medicinal Chemistry* **2020,** *11* (8), 858-875.
43. Ciardiello, D.; Vitiello, P. P.; Cardone, C.; Martini, G.; Troiani, T.; Martinelli, E.; Ciardiello, F., Immunotherapy of colorectal cancer: Challenges for therapeutic efficacy. *Cancer Treatment Reviews* **2019,** *76*, 22-32.
44. Battogtokh, G.; Cho, Y.-Y.; Lee, J. Y.; Lee, H. S.; Kang, H. C., Mitochondrial-Targeting Anticancer Agent Conjugates and Nanocarrier Systems for Cancer Treatment. *Frontiers in Pharmacology* **2018,** *9*, 922.
45. Zheng, B.-X.; Long, W.; She, M.-T.; Wang, Y.; Zhao, D.; Yu, J.; Siu-Lun Leung, A.; Hin Chan, K.; Hou, J.; Lu, Y.-J.; Wong, W.-L., A Cytoplasm-Specific Fluorescent Ligand for Selective Imaging of RNA G-Quadruplexes in Live Cancer Cells. *Chemistry – A European Journal* **2023,** *29* (34), e202300705.
46. Modica-Napolitano, J. S.; Weissig, V., Treatment Strategies that Enhance the Efficacy and Selectivity of Mitochondria-Targeted Anticancer Agents. *International Journal of Molecular Sciences* **2015,** *16* (8), 17394-17421.
47. del Villar-Guerra, R.; Trent, J. O.; Chaires, J. B., G-Quadruplex Secondary Structure Obtained from Circular Dichroism Spectroscopy. *Angewandte Chemie International Edition* **2018,** *57* (24), 7171-7175.
48. Tran, Phong Lan T.; Rieu, M.; Hodeib, S.; Joubert, A.; Ouellet, J.; Alberti, P.; Bugaut, A.; Allemand, J.-F.; Boulé, J.-B.; Croquette, V., Folding and persistence times of intramolecular G-quadruplexes transiently embedded in a DNA duplex. *Nucleic Acids Research* **2021,** *49* (9), 5189-5201.
49. Park, K.-S.; Jo, I.; Pak, Y.; Bae, S.-W.; Rhim, H.; Suh, S.-H.; Park, S.; Zhu, M.; So, I.; Kim, K., FCCP depolarizes plasma membrane potential by activating proton and Na+ currents in bovine aortic endothelial cells. *Pflügers Archiv* **2002,** *443* (3), 344-352.

50. Gizatullina, Z. Z.; Gaynutdinov, T. M.; Svoboda, H.; Jerzembek, D.; Knabe, A.; Vielhaber, S.; Malesevic, M.; Heinze, H. J.; Fischer, G.; Striggow, F.; Gellerich, F. N., Effects of cyclosporine A and its immunosuppressive or non-immunosuppressive derivatives [D-Ser]8-CsA and Cs9 on mitochondria from different brain regions. *Mitochondrion* **2011,** *11* (3), 421-429.
51. Schultz, K.; Murthy, V.; Tatro, J. B.; Beasley, D., Prolyl hydroxylase 2 deficiency limits proliferation of vascular smooth muscle cells by hypoxia-inducible factor-1{alpha}-dependent mechanisms. *Am J Physiol Lung Cell Mol Physiol* **2009,** *296* (6), L921-927.
52. Aquino-Gálvez, A.; González-Ávila, G.; Delgado-Tello, J.; Castillejos-López, M.; Mendoza-Milla, C.; Zúñiga, J.; Checa, M.; Maldonado-Martínez, H. A.; Trinidad-López, A.; Cisneros, J.; Torres-Espíndola, L. M.; Hernández-Jiménez, C.; Sommer, B.; Cabello-Gutiérrez, C.; Gutiérrez-González, L. H., Effects of 2-methoxyestradiol on apoptosis and HIF-1α and HIF-2α expression in lung cancer cells under normoxia and hypoxia. *Oncol Rep* **2016,** *35* (1), 577-583.
53. Narita, T.; Yin, S.; Gelin, C. F.; Moreno, C. S.; Yepes, M.; Nicolaou, K. C.; Van Meir, E. G., Identification of a Novel Small Molecule HIF-1α Translation Inhibitor. *Clinical Cancer Research* **2009,** *15* (19), 6128-6136.
54. Bannwarth, S.; Berg-Alonso, L.; Augé, G.; Fragaki, K.; Kolesar, J. E.; Lespinasse, F.; Lacas-Gervais, S.; Burel-Vandenbos, F.; Villa, E.; Belmonte, F.; Michiels, J.-F.; Ricci, J.-E.; Gherardi, R.; Harrington, L.; Kaufman, B. A.; Paquis-Flucklinger, V., Inactivation of Pif1 helicase causes a mitochondrial myopathy in mice. *Mitochondrion* **2016,** *30*, 126-137.
55. Bharti, S. K.; Sommers, J. A.; Zhou, J.; Kaplan, D. L.; Spelbrink, J. N.; Mergny, J.-L.; Brosh, R. M., DNA Sequences Proximal to Human Mitochondrial DNA Deletion Breakpoints Prevalent in Human Disease Form G-quadruplexes, a Class of DNA Structures Inefficiently Unwound by the Mitochondrial Replicative Twinkle Helicase*. *Journal of Biological Chemistry* **2014,** *289* (43), 29975-29993.
56. Pietras, Z.; Wojcik, M. A.; Borowski, L. S.; Szewczyk, M.; Kulinski, T. M.; Cysewski, D.; Stepien, P. P.; Dziembowski, A.; Szczesny, R. J., Dedicated surveillance mechanism controls G-quadruplex forming non-coding RNAs in human mitochondria. *Nature Communications* **2018,** *9* (1), 2558.
57. Rodier, F.; Campisi, J., Four faces of cellular senescence. *Journal of Cell Biology* **2011,** *192* (4), 547-556.
58. He, S.; Sharpless, N. E., Senescence in Health and Disease. *Cell* **2017,** *169* (6), 1000-1011.
59. Miwa, S.; Kashyap, S.; Chini, E.; von Zglinicki, T., Mitochondrial dysfunction in cell senescence and aging. *J Clin Invest* **2022,** *132* (13), e158447.
60. Freund, A.; Laberge, R.-M.; Demaria, M.; Campisi, J., Lamin B1 loss is a senescence-associated biomarker. *Molecular Biology of the Cell* **2012,** *23* (11), 2066-2075.
61. Szewczyk-Golec, K.; Pawłowska, M.; Wesołowski, R.; Wróblewski, M.; Mila-Kierzenkowska, C., Oxidative Stress as a Possible Target in the Treatment of Toxoplasmosis: Perspectives and Ambiguities. *International Journal of Molecular Sciences* **2021,** *22* (11), 5705.
62. Zhang, Y.; Su, S. S.; Zhao, S.; Yang, Z.; Zhong, C.-Q.; Chen, X.; Cai, Q.; Yang, Z.-H.; Huang, D.; Wu, R.; Han, J., RIP1 autophosphorylation is promoted by mitochondrial ROS and is essential for RIP3 recruitment into necrosome. *Nature Communications* **2017,** *8* (1), 14329.
63. Chen, Z.; Ho, I. L.; Soeung, M.; Yen, E.-Y.; Liu, J.; Yan, L.; Rose, J. L.; Srinivasan, S.; Jiang, S.; Edward Chang, Q.; Feng, N.; Gay, J. P.; Wang, Q.; Wang, J.; Lorenzi, P. L.; Veillon, L. J.; Wei, B.; Weinstein, J. N.; Deem, A. K.; Gao, S.; Genovese, G.; Viale, A.; Yao, W.; Lyssiotis, C. A.; Marszalek, J. R.; Draetta, G. F.; Ying, H., Ether phospholipids are required for mitochondrial reactive oxygen species homeostasis. *Nature Communications* **2023,** *14* (1), 2194.
64. Shi, L.; Tu, B. P., Acetyl-CoA and the regulation of metabolism: mechanisms and consequences. *Curr Opin Cell Biol* **2015,** *33*, 125-131.
65. Aguer, C.; Gambarotta, D.; Mailloux, R. J.; Moffat, C.; Dent, R.; McPherson, R.; Harper, M. E., Galactose enhances oxidative metabolism and reveals mitochondrial dysfunction in human primary muscle cells. *PLoS One* **2011,** *6* (12), e28536.
66. Mejia, E. M.; Hatch, G. M., Mitochondrial phospholipids: role in mitochondrial function. *J Bioenerg Biomembr* **2016,** *48* (2), 99-112.